Evaluating Annual Precipitation Extremes in the U.S. Great Plains using PRISM Data

Authors: Sumiaya Amin Preota[1,2], Gaurav Talukdar[1], Sam Zipper[1,3,*]

Affiliations:

[1] Kansas Geological Survey, University of Kansas, Lawrence, Kansas
[2] School of Earth, Environmental, and Marine Sciences, University of Texas Rio Grande Valley, Texas
[3] Department of Geology, University of Kansas, Lawrence, Kansas
* Correspondence to Sam Zipper, samzipper@ku.edu

Abstract

Understanding hydroclimatic extremes in the U.S. Great Plains (USGP) is crucial for effective water resource management, resiliency of agricultural systems, and mitigation of climate change impacts. This study examines changing hydroclimatic conditions in the USGP, with a focus on annual-resolution precipitation trends and extremes over the past 119 years (1904–2022) using precipitation data from the gridded PRISM climate dataset. We categorized annual-scale precipitation totals into six categories of hydroclimatic extremes: (1) isolated wet extremes, (2) isolated dry extremes, (3) dry-to-dry recurring extremes, (4) wet-to-wet recurring extremes, (5) dry-to-wet whiplash extremes, and (6) wet-to-dry whiplash extremes. "Recurring" and "whiplash" are both types of compound extremes. To assess the accuracy of the PRISM data, we first compared annual PRISM precipitation totals to meteorological stations across the region. We found a strong correlation ($R^2 \geq 0.75$) at 251 out of 257 stations and little overall bias, indicating that the PRISM data are reliable for regional-scale characterization of annual precipitation dynamics. Looking at annual precipitation totals, we observed significant increasing trends over much of the eastern and northern USGP. Looking at hydroclimatic extremes, we observed that isolated wet and dry extremes tend to be fairly uniformly distributed across the USGP, while compound extremes show more pronounced spatial patterns. Dry-to-dry recurring extremes are most prevalent in South Dakota and the Kansas-Colorado-Texas-Oklahoma border region, while wet-to-wet recurring extremes are most common in Minnesota, Iowa, Nebraska, and the North Dakota-South Dakota border region. These findings have significant implications for water resource management and agricultural systems in the U.S. Great Plains, highlighting the need for adaptive strategies to address changing hydroclimatic conditions.

Funding and Acknowledgments

This work was supported by USDA NIFA AFRI grant no. 2022-67019-37181 and Kansas Water Office contract #25-113. We thank the National Centers for Environmental Information (NCEI) and PRISM Climate Group of Oregon State University for publicly sharing the GHCND data and geospatial data set. This is the final report for Sumiaya Amin Preota as a participant in the Kansas Geological Survey's Geohydrology Internship Program (http://www.kgs.ku.edu/Hydro/gipIndex.html). Portions of this work were presented as part of a conference poster at the 2024 AGU Fall Meeting.

1. Introduction

Hydroclimatic extremes are severe weather conditions that can significantly harm both natural ecosystems and human systems. Heat waves, floods, droughts, and excessive precipitation are known as hydroclimatic extremes, and past work has shown these types of extremes have significantly increased in frequency and intensity due to anthropogenic activities (Wang et al., 2022). Compound extremes, which are combinations of multiple extremes either in space or time (Hao et al., 2018), can have particularly severe consequences on hydrologic processes and various sectors such as water treatment, reservoir operations, and agriculture. Compound hydroclimatic extremes can include the same type of extreme recurring in time (i.e., wet-to-wet or dry-to-dry patterns) and shifts from one type of extreme to another (wet-to-dry and dry-to-wet patterns, previously termed “weather whiplash”) (Loecke et al., 2017; Na and Najafi, 2024).

Many major U.S. crops, such as corn, soybeans, wheat, cotton, and sorghum, are grown in the U.S. Great Plains (USGP) region, and hydroclimatic extremes imperil their production (Kaur et al., 2020; Zipper et al., 2016). As a result, hydroclimatic extremes—whether isolated or compound in nature—present challenges for water management and agriculture in the USGP. Both excessive and insufficient precipitation can lead to negative outcomes, such as floods and crop damage. Excessive precipitation can cause waterlogging of soils, particularly in areas of shallow groundwater, which reduces oxygen availability to plant roots and can lead to root diseases and yield loss (Booth et al., 2016; Zipper et al., 2015). The increased runoff from intense precipitation can also carry away topsoil and nutrients, diminishing soil fertility and agricultural productivity. In contrast, insufficient precipitation can lead to yield losses in rainfed crops or increased irrigation water demands, imperiling water resources (Whittemore et al., 2023; Zipper et al., 2016, 2022). Recurring extremes, such as consecutive years of drought or high precipitation, can have cumulative effects that strain resources and reduce resilience. Weather whiplash events, where rapid transitions occur between wet and dry conditions (Loecke et al., 2017; Na and Najafi, 2024), can be particularly disruptive, as systems designed to cope with one extreme may struggle to adjust to the opposite condition.

Both isolated and compound hydroclimatic extremes are hard to predict using climate models (Sillmann et al., 2017). Therefore, evaluating historical trends and patterns in hydroclimatic extremes offers valuable clues for anticipating how these extremes are changing and their potential impacts on the future of agricultural and water management systems in the region. To address this, we evaluate regional spatial patterns and long-term changes in annual-resolution precipitation extremes across the USGP region using gridded precipitation data from the Parameter-elevation Regressions on Independent Slopes Model (PRISM) dataset (PRISM Climate Group, 2024). These data were used to address the following objectives:

1. Assess the reliability of gridded PRISM data by comparing it to regional meteorological station-based data.
2. Analyze long-term trends in annual precipitation across the USGP.
3. Evaluate the spatial and temporal patterns of changing annual-scale precipitation extremes.

2. Study Area

The USGP is a vast region that extends across the central United States (fig. 1), from the Canadian border down to Texas and from the Rocky Mountains to the Mississippi River, encompassing significant spatiotemporal variability in rainfall, hydrology, agriculture, and ecosystems. The USGP is a crucial agricultural zone, producing large amounts of wheat, corn, soybeans, and livestock, and as a result it is highly susceptible to hydroclimatic extremes such as droughts, floods, and extreme temperature fluctuations.

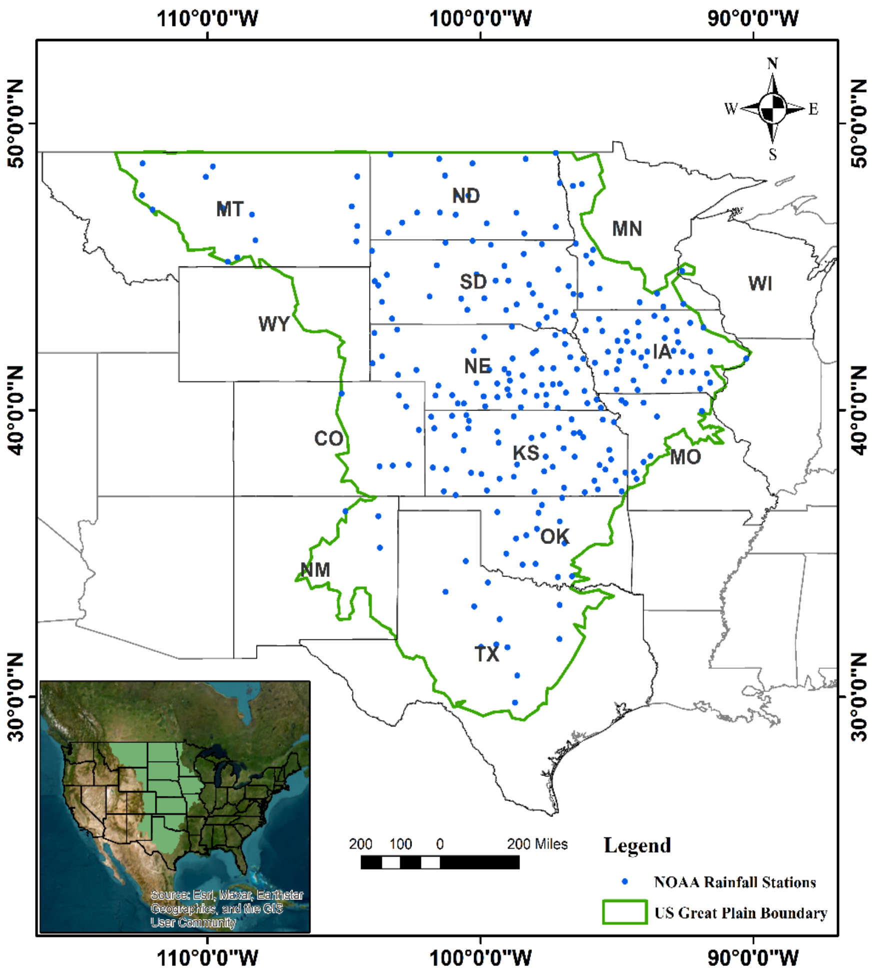

Figure 1. Map of the USGP study area boundary including locations of Global Historical Climatology Network daily (GHCND) weather stations used in this study.

Droughts are a recurring feature of the Great Plains, driven by large-scale atmospheric patterns such as La Niña, which induces prolonged periods of below-average rainfall (Schubert et al., 2004). These dry spells can severely impact agricultural productivity, water resources, and natural ecosystems. The Dust Bowl of the 1930s exemplifies extreme drought, exacerbated by unsustainable land management practices, leading to massive soil erosion and socio-economic upheaval. Contemporary droughts continue to pose significant risks, necessitating advanced water management and conservation strategies to mitigate their impacts (Whittemore et al., 2023; Zipper et al., 2016). Conversely, the Great Plains also experiences episodes of intense precipitation and flooding, driven by phenomena such as the North American Monsoon and mesoscale convective systems (Na et al., 2022). Extreme precipitation can lead to rapid increases in river discharge, overwhelming flood control infrastructure and causing substantial damage to communities, agriculture, and infrastructure.

3. Methodology

Figure 2 shows the overarching workflow to address the three objectives of our study. The project was conducted using ArcMap and RStudio software for data analysis and visualization.

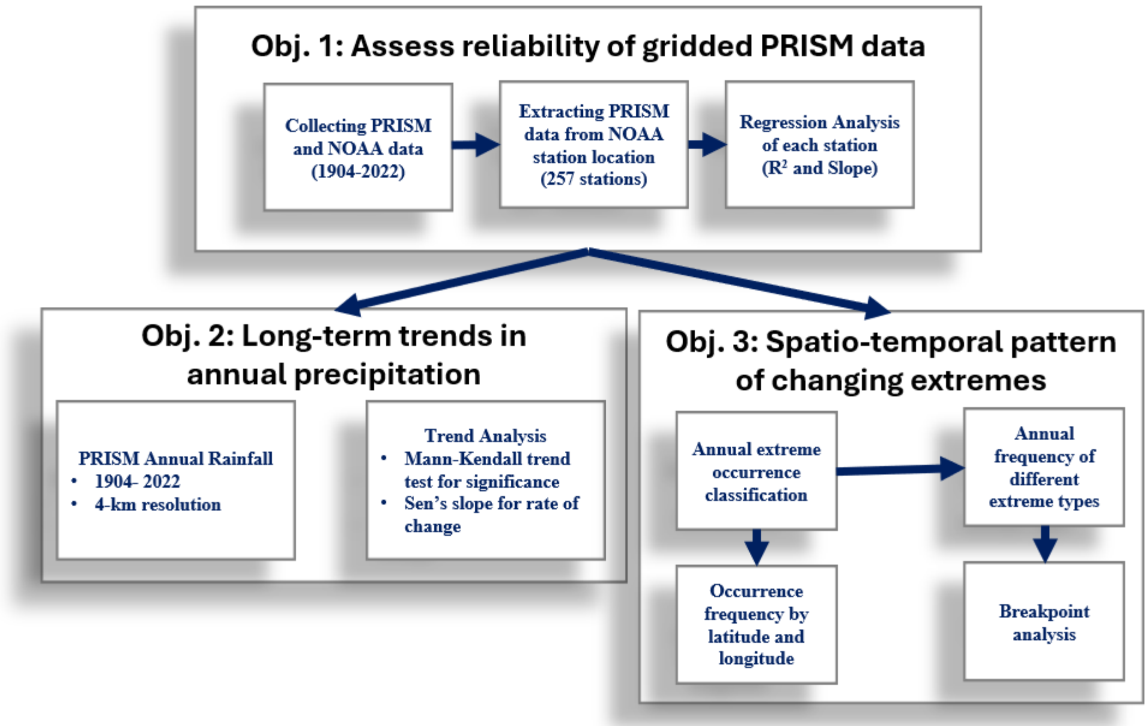

Figure 2. Flowchart of the analysis, including different data processing steps and outputs.

3.1 PRISM meteorological data and comparison with GHCND station data

We used PRISM data for our regional analysis due to its continuous spatial and temporal coverage. PRISM is a high-resolution (4 km grid cells) spatial climate data product that provides information about mean temperature, precipitation, maximum/minimum temperatures, and dewpoint for the United States (PRISM Climate Group, 2024). The gridded dataset is created using data from 13,000 precipitation and 10,000 temperature stations, and factors such as location, elevation, coastal proximity, atmospheric structure, topographic position/orientation, and orographic effects of the terrain are used to interpolate between stations and create the gridded product (Daly et al., 2008). For our annual-scale analysis, we downloaded, stacked, and summed monthly precipitation PRISM data for the 1904–2022 period for the USGP region.

Because gridded meteorological data can obscure or average out important weather features (Mourtzinis et al., 2017), we assessed the reliability of annual precipitation depth from PRISM via comparison to 257 meteorological stations (fig. 1) from the Global Historical Climatology Network daily (GHCND) precipitation station dataset (available online at https://www.ncei.noaa.gov/products/land-based-station/global-historical-climatology-network-daily). Weather stations were selected based on having at least 90% of data available during the 1904–2022 study period; a separate research project is investigating station-based trends in precipitation and annual hydroclimatic extremes. GHCND is maintained by the National Oceanic and Atmospheric Administration's National Centers for Environmental Information (NOAA NCEI). Because GHCND station data are point based, these point locations were used to extract the values from PRISM raster data over the years. The extracted PRISM and GHCND precipitation values were then used in a linear regression analysis for each station over the years to evaluate the agreement between these two data sources.

3.2 Spatio-temporal analysis of precipitation and extremes

We evaluated changes in both mean annual precipitation and different types of annual-resolution precipitation extremes. All analyses were done for each PRISM grid cell within the USGP region. For investigating changes in mean annual precipitation, we evaluated trend significance using the non-parametric Mann-Kendall test (i.e., Zipper et al., 2021) and the magnitude of trends using Sen's slope (fig. 2). We also visualized average annual rainfall at 10-year and 30-year intervals to visually inspect any decadal changes within the study area.

To investigate changing hydroclimatic extremes, we categorized annual-resolution precipitation totals into six typologies: (1) isolated wet extremes, (2) isolated dry extremes, (3) dry-to-dry recurring extremes, (4) wet-to-wet recurring extremes, (5) dry-to-wet whiplash extremes, and (6) wet-to-dry whiplash extremes. "Recurring" and "whiplash" are both types of compound extremes. All extremes were identified using the percentile of the annual precipitation, calculated at pixel-resolution for 1904–2022 from the PRISM data. We first identified extreme years based on whether the annual precipitation percentiles were < 20 (dry extreme) or > 80 (wet extreme). We then defined recurring extremes as consecutive years with the same extreme type, and whiplash changes for consecutive years where there was a year-over-year change in percentile of at least 60. Isolated extremes were then identified as remaining extreme years that were not part of either a recurring or whiplash compound extreme. We elected to use a percentile-based approach because it is transferable across our entire region since it defines extremes based on the historic conditions at each individual location (Facincani Dourado et al., 2024; Swain et al., 2018). We created annual rasters for each of the six extreme types, with a pixel experiencing that extreme type in that year identified with a value of 1 and a pixel not experiencing that extreme type identified with a value of 0.

To summarize spatial patterns, we binned the grid cells into 3° intervals with respect to latitude and longitude and plotted the distribution within each bin. To investigate changes in extremes through time, we investigated aggregated regional trends in extreme occurrence through time by looking at the percentage of the total domain experiencing each extreme type in each year. Breakpoint analysis was conducted to observe how the extremes have changed over time. The "*strucchange*" package in R was used to perform the breakpoint analysis. This method identifies structural changes within time series data by detecting significant changes in the mean of the residuals. The package was used with its default parameters, including a minimum segment size of 15% of samples (i.e., ~18 years for our 117 year study period), a maximum of four allowed breakpoints, and breaks defined sequentially. Therefore, it should represent an initial assessment of potential breakpoints but not a definitive or comprehensive analysis of breakpoint occurrence or timing. For extreme typologies where breakpoints were identified, we looked at spatial patterns by mapping the total occurrences as a fraction of the period length.

4. Results & Discussion

4.1 Comparison between PRISM gridded data and GHCND station data

The result of a linear regression between the GHCND and PRISM precipitation data showed strong agreement ($R^2 \geq 0.75$) in 251 out of 257 stations (figs. 3a and 4a), suggesting that the PRISM data are capturing the majority of the variability in the station data. One station had extremely low R^2 ($R^2 < 0.22$). However, it is close to another station with a reasonable R^2, suggesting an issue with this station's data rather than the PRISM data.

We also examined the slope value to see whether the station data were consistently overestimated or underestimated. In the regressions, annual precipitation from the GHCND stations was the dependent (y-axis) variable, and therefore a slope > 1 would indicate station-based precipitation totals are higher than PRISM data and a slope < 1 would indicate station-based precipitation totals are lower than PRISM data. Most slopes were slightly > 1 (figs. 3b and 4b), indicating that the PRISM data may slightly underestimate annual precipitation relative to the station data. Out of the 251 stations with $R^2 > 0.75$, 246 have a slope value between 0.85 and 1.15, or agreement within 15%. This indicates a consistently strong agreement between the two precipitation data sources, and the slope range close to 1 suggests that the PRISM data are reliable enough to be used as a gridded source for estimating precipitation over the Great Plains in a spatially and temporally continuous manner. Furthermore, since the identification of extremes is percentile-based, we would not expect this to hinder our ability to identify years with extreme high or low precipitation depths. The appendix of this report provides a list of the location-wise R^2 and slope values (table A1).

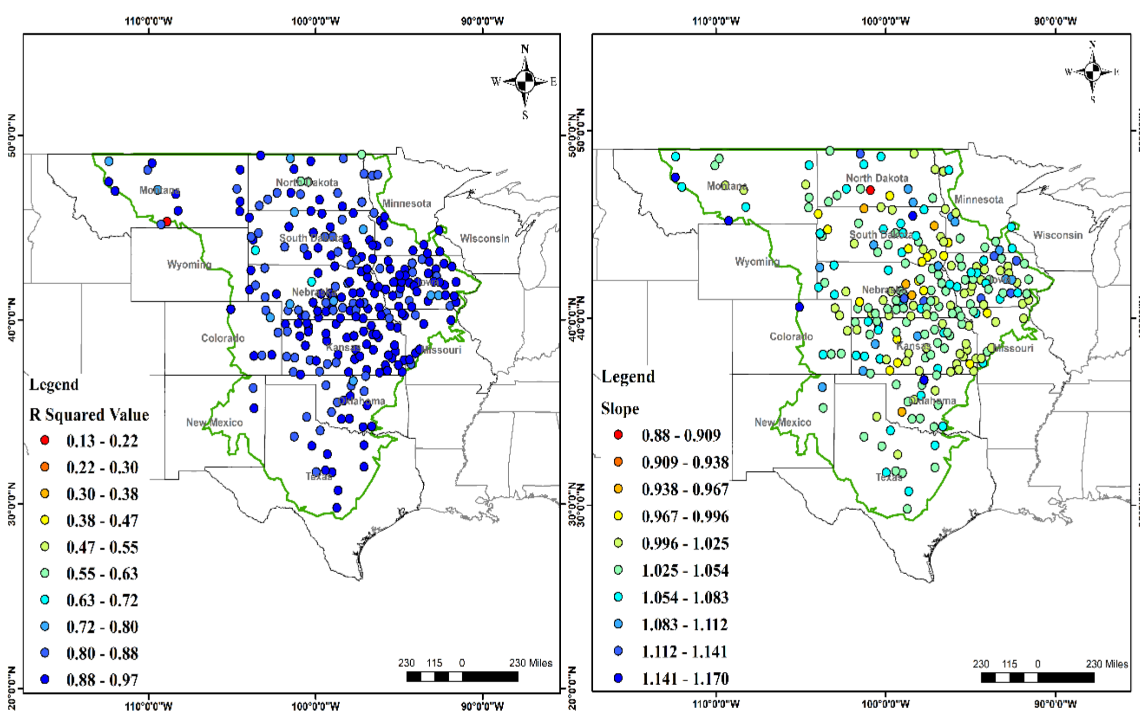

(a) (b)

Figure 3. (a) R^2 and (b) slope value for comparison between GHCND and PRISM at each meteorological station location.

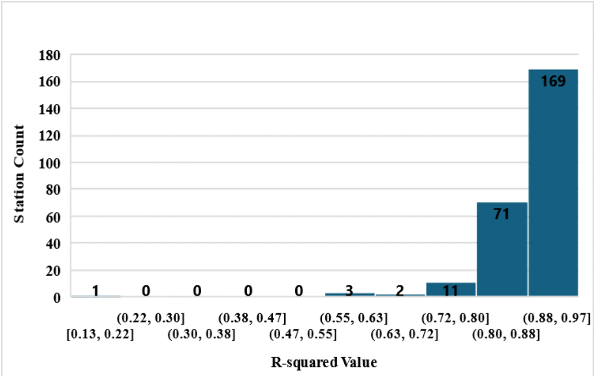

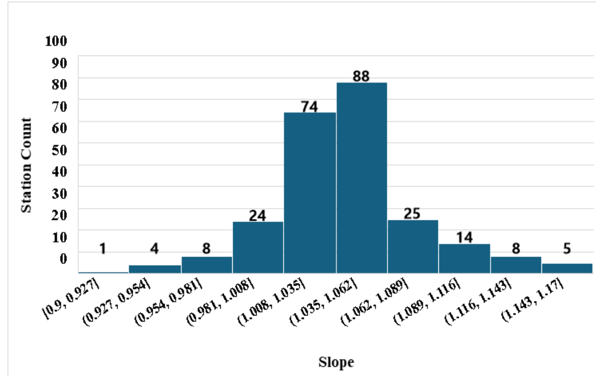

(a) **(b)**

Figure 4. Distribution of the (a) R^2 and (b) slope values for comparison between GHCND and PRISM across all meteorological stations.

4.2 Spatial and temporal patterns of annual precipitation

The average annual precipitation (1904–2022) ranges widely across the USGP, with higher rainfall in the eastern portion of region compared to the western portion (fig. 5). Visually, the average annual rainfall calculated over 30-year intervals did not show any major patterns (fig. A1), but averaging over 10-year intervals shows decadal variability in rainfall (fig. A2). Decades that appear drier include the 1930s, 1950s, 1980s, and 2000s, while decades that appear wetter include the 1940s, 1960s, 1970s, and 1990s. These maps provide visuals of potential patterns, and our following trend analyses are able to identify where significant changes have occurred through time.

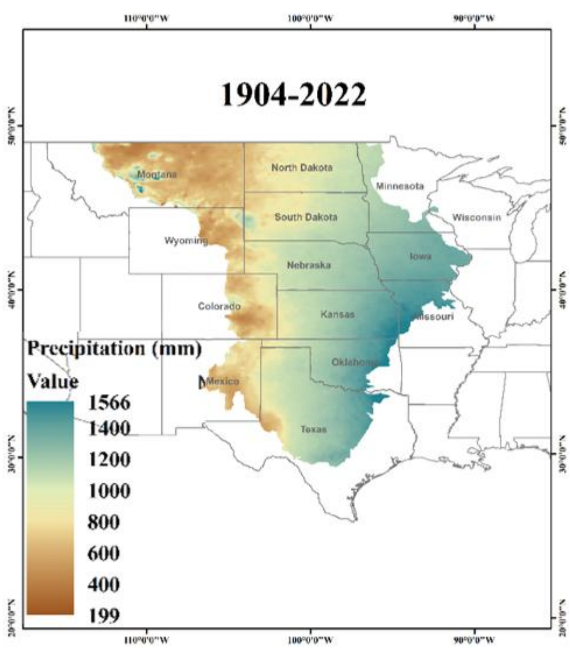

Figure 5. Mean annual precipitation for each grid cell in the study region.

The non-parametric Mann-Kendall trend analysis showed that the region is generally wetting (positive Tau [τ] value), in particular the already-wet eastern portions of the domain, with a few isolated locations of drying (negative τ) in the western portion of the USGP (fig. 6a). However, very few drying trends are significant, with only a few pixels in the northwestern portion of the domain showing trends toward lower mean annual precipitation (fig. 6b). The Sen's slope analysis provides an indication of the strength of these trends, with changes up to about 2 mm/yr (fig. 6b). Importantly, this analysis only investigates changes in precipitation, which represents the atmospheric supply of water, but does not account for potential increases in atmospheric water demand due to warming-driven increases in potential evapotranspiration (PET). Past regional analyses have suggested that increases in PET may overwhelm changes in precipitation, leading to a net aridification in the region despite the increasing precipitation trend in much of the domain (Seager, Feldman, et al., 2017; Seager, Lis, et al., 2017). In Kansas, for example, there is a statewide trend toward warmer conditions (Lin et al., 2017), which would lead to an increase in PET. An important direction for future work is investigating the relative strength of trends in precipitation and PET to determine whether there is a net increase or decrease in overall aridity within the USGP region.

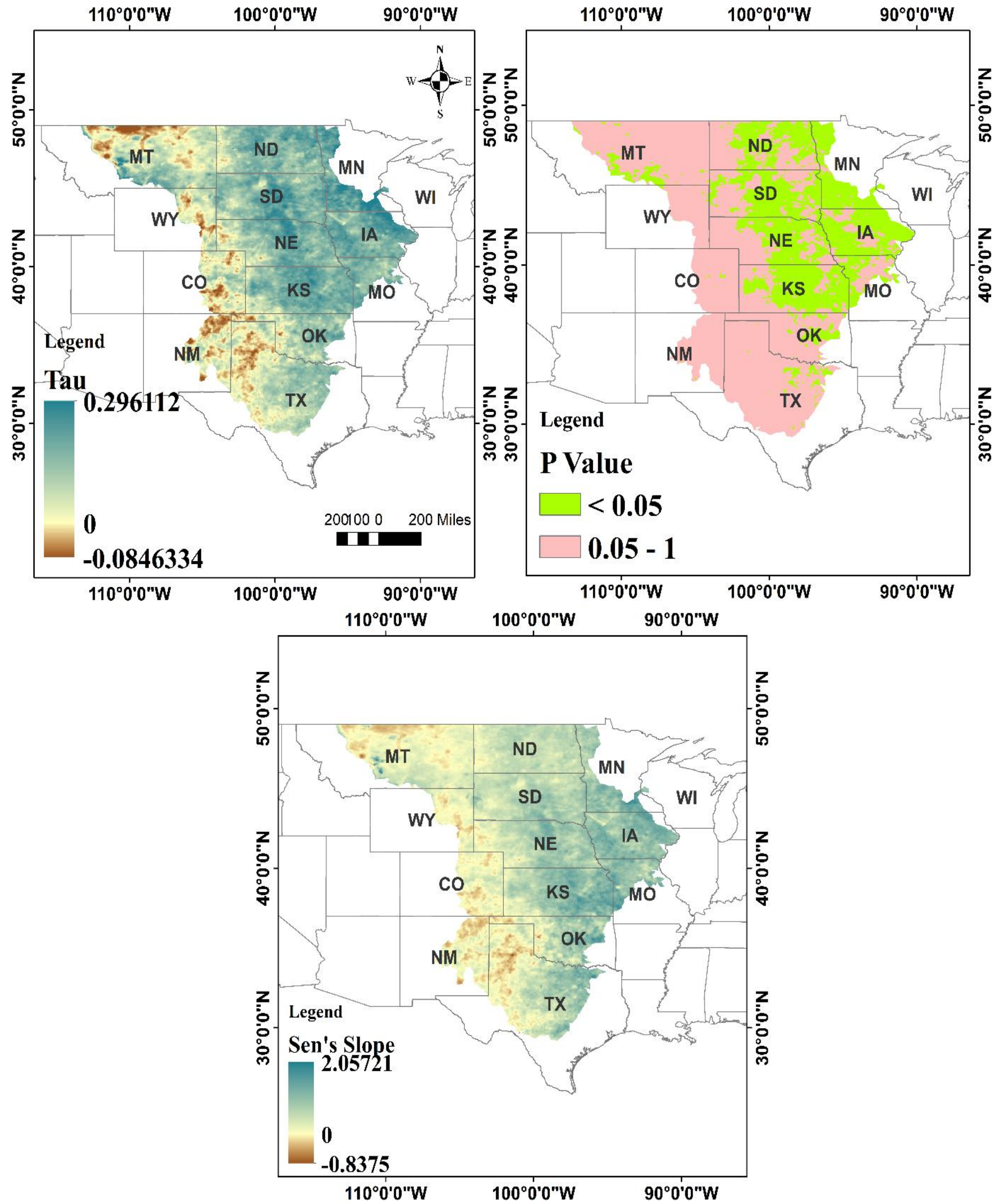
110°0'0"W
100°0'0"W
90°0'0"W
50°0'0"N
40°0'0"N
30°0'0"N
N
S
W
E
MT
ND
MN
SD
WI
WY
IA
NE
CO
KS
MO
OK
NM
TX
Legend
Tau
0.296112
0
-0.0846334
200100 0 200 Miles
Legend
P Value
< 0.05
0.05 - 1
Legend
Sen's Slope
2.05721
0
-0.8375

(a)

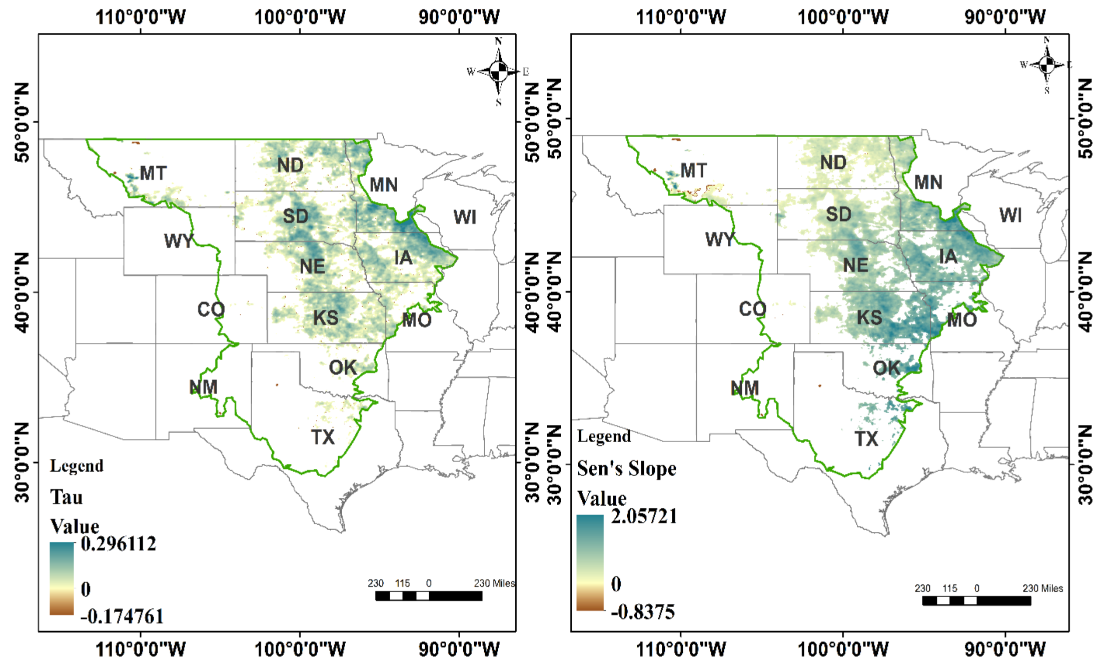

(b)

Figure 6. (a) Mann-Kendell trend analysis (Tau and p-value) and Sen's slope analysis for entire domain; (b) Tau and Sen's slope value for only pixels with a significant ($p < 0.05$) change identified by the Mann-Kendall test.

4.3 Spatial patterns of annual precipitation extremes

The six different types of annual precipitation extremes we calculated had distinct spatial patterns across the USGP (fig. 7). Isolated dry extremes (defined as a year with < 20th percentile precipitation and not part of a compound recurring or whiplash extreme) have occurred most frequently in the northwest, southwest, and southeast portions of the USGP. In contrast, isolated wet extremes (defined as a year with > 80th percentile precipitation and not part of a compound recurring or whiplash extreme) have occurred most frequently in the northern, eastern, and western USGP. Recurring extremes (consecutive dry or wet extremes) are relatively less frequent than isolated or whiplash extremes but have the most distinct spatial patterns. Dry-to-dry extremes have occurred most frequently in the Texas-Oklahoma panhandle region, South Dakota, and much of Montana and Kansas. In contrast, wet-to-wet extremes have occurred most frequently in Iowa, South Dakota, and Nebraska. Whiplash extremes (year-to-year changes exceeding 60 percentile points) are more common than recurring extremes but less frequent than isolated extremes. Dry-to-wet extremes have occurred most frequently in parts of Texas, Colorado, and North Dakota, and wet-to-dry extremes have occurred most frequently in North Dakota, Colorado, and Missouri.

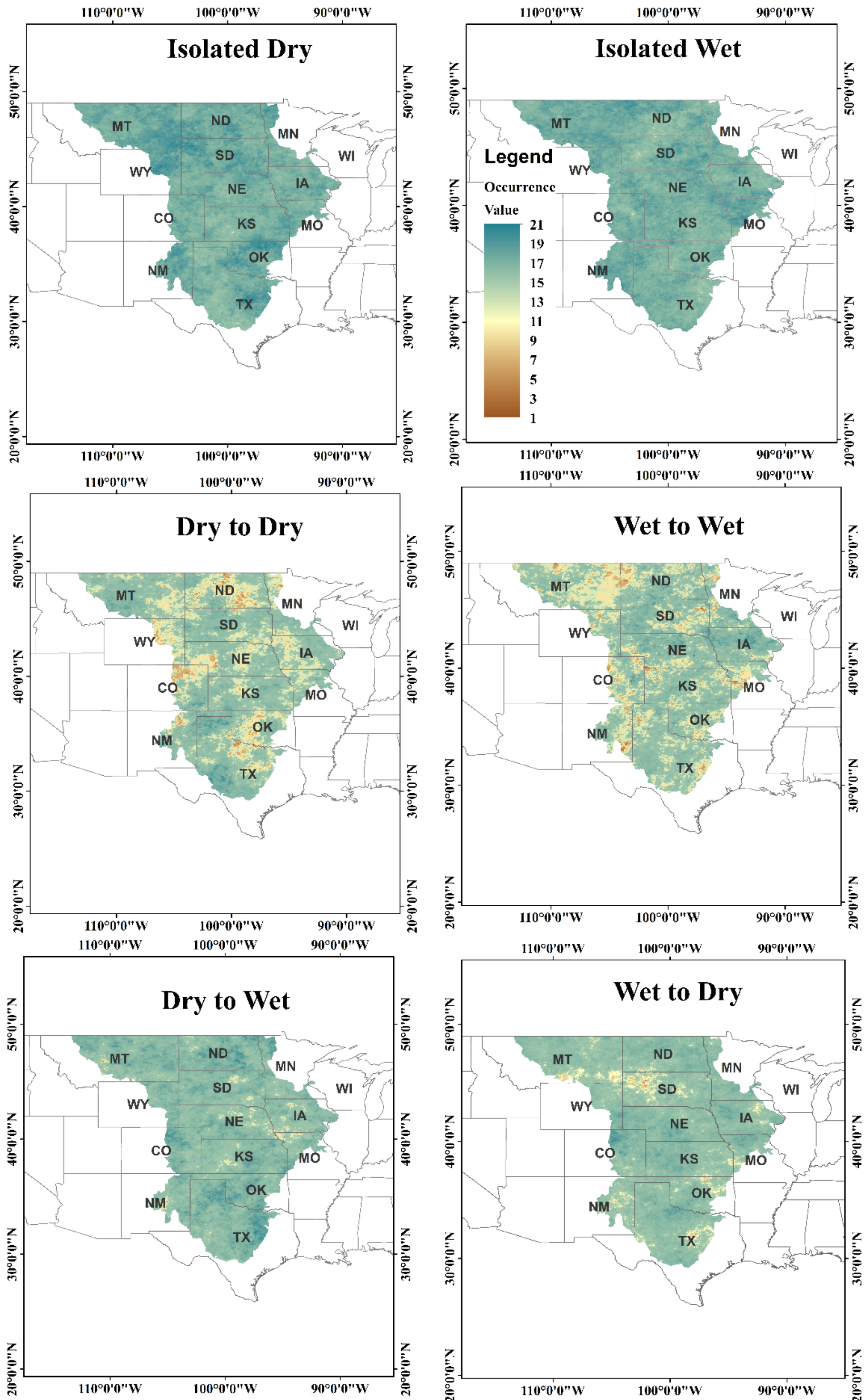

Figure 7. Number of occurrences for each type of hydroclimatic extreme for the 1904–2022 study period.

Distributions of extreme occurrences binned by latitude and longitude (figs. 8 and 9) were created to further investigate the spatial distribution of each type of extreme. In general, the patterns are consistent with what was discussed related to the map, and there is more variability within the longitude bins (fig. 9) than the latitude bins (fig. 8). The isolated dry occurrences were greatest in the bins of latitudes from 32.5–35.5° N and 44.5–50.5° N, and longitudes from -103 to -109° E. In contrast, isolated wet occurrences tended to increase at higher latitudes and were the greatest from -103 to -112° E longitude. Wet-to-wet compound extremes tended to be most prevalent toward eastern latitudes, while dry-to-dry compound extremes were most prevalent at western latitudes. Whiplash extremes tended to be greatest for both dry-to-wet and wet-to-dry at the easternmost and westernmost portions of the study region. However, wet-to-dry extremes tended to be greatest at middle latitudes (38.5 to 41.5° N), and dry-to-wet extremes tended to be greatest at the farthest south (29.5–35.5° N) and farthest north (44.5–50.5° N) latitude bins. Differences among bins were not tested for statistical significance, so it is not known whether the patterns described here are statistically significant or not.

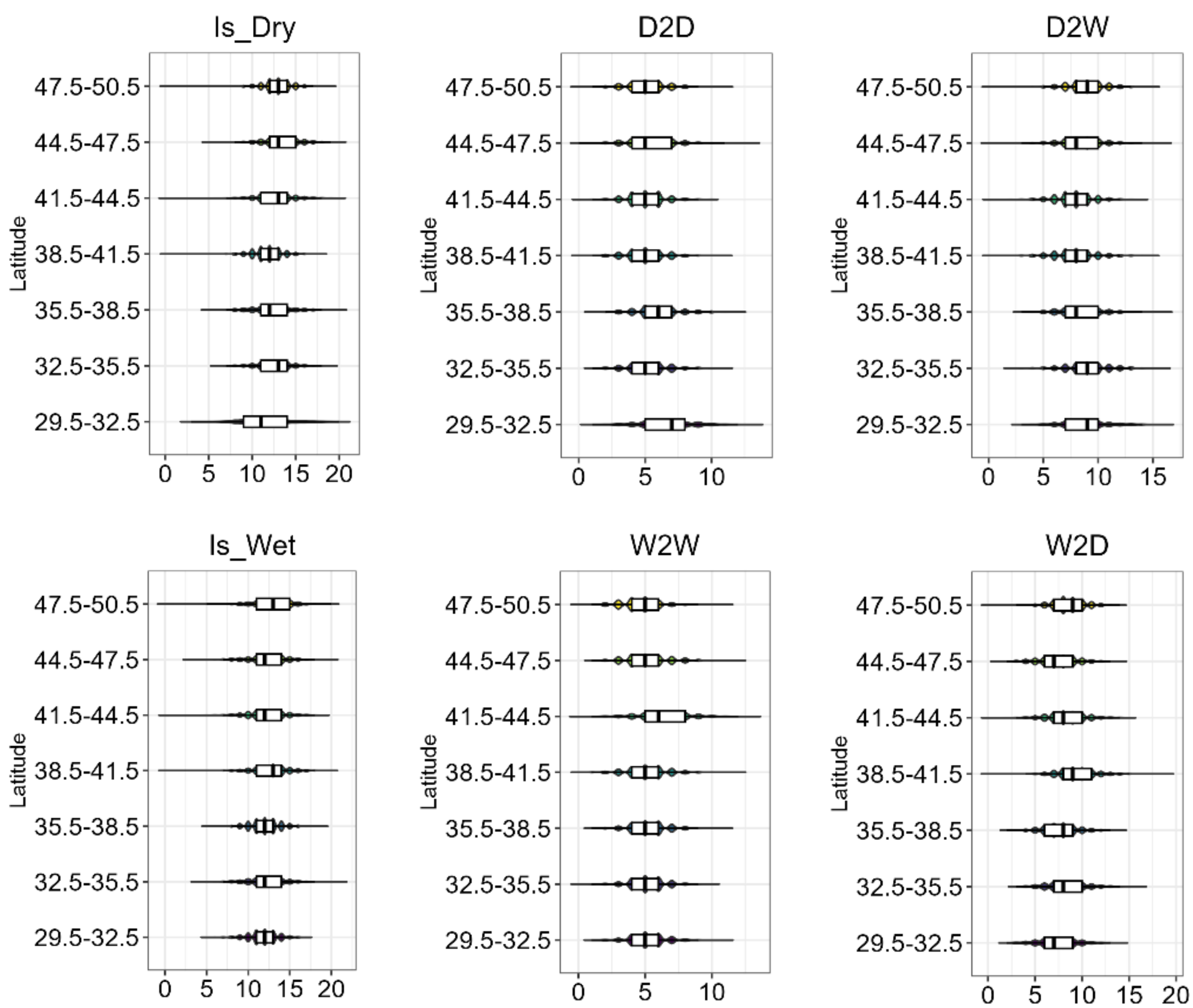

Figure 8. Number of occurrences for each extreme type during the 1904–2022 study period, binned by latitude (°N). Is_Dry = isolated dry, Is_Wet = isolated wet, D2D = dry-to-dry, W2W = wet-to-wet, D2W = dry-to-wet, W2D = wet-to-dry.

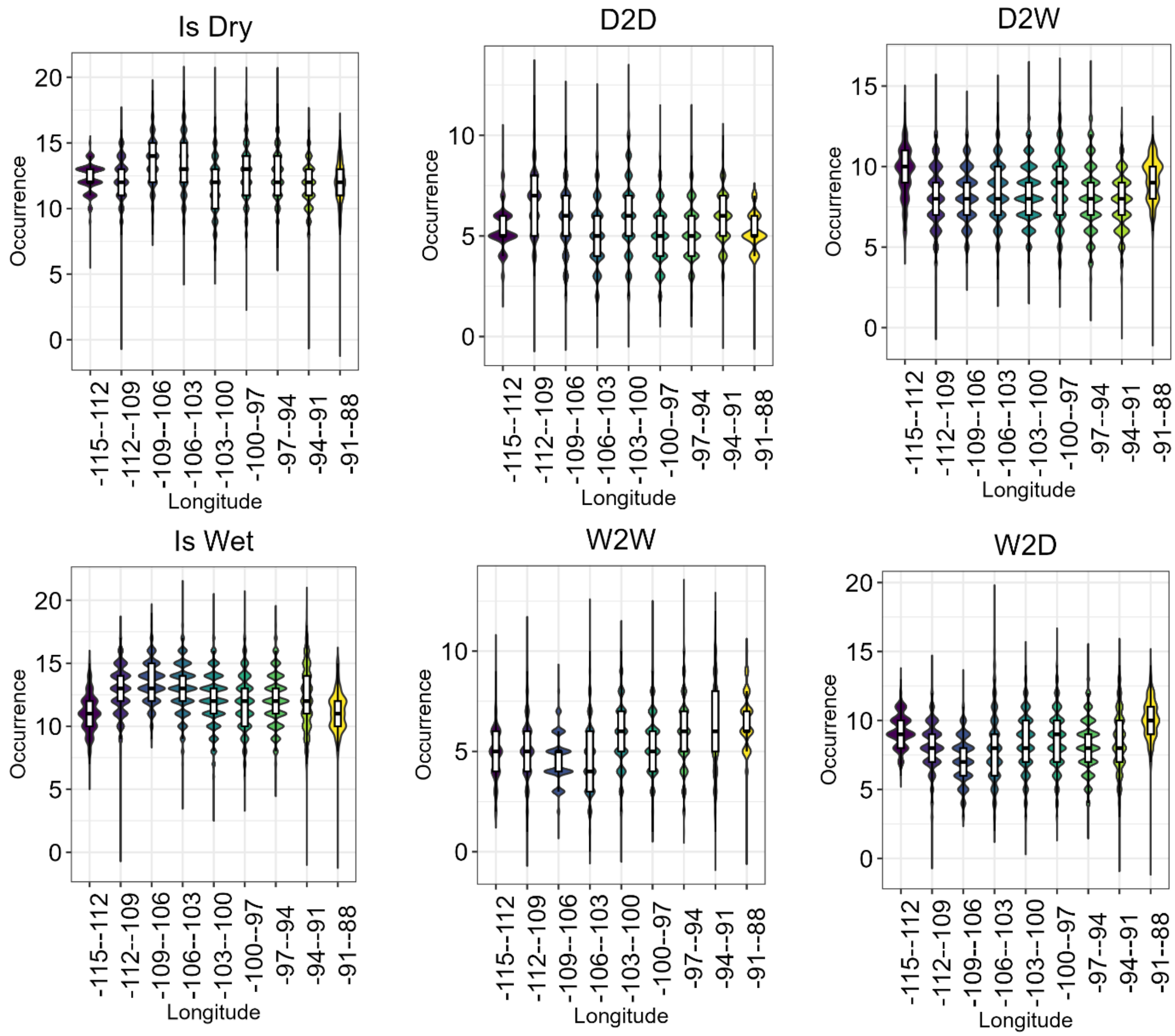

Figure 9. Number of occurrences for each extreme type during the 1904-2022 study period, binned by longitude (°E). Is Dry = isolated dry, Is Wet = isolated wet, D2D = dry-to-dry, W2W = wet-to-wet, D2W = dry-to-wet, W2D = wet-to-dry.

4.4 Temporal changes of annual precipitation extremes

We investigated aggregated regional trends in each type of extreme by quantifying changes in the percent of pixels within the study domain experiencing each extreme type in each year and tested for trends and potential breakpoints within each time series (fig. 10). Overall, isolated dry extremes showed a marginally non-significant decreasing tendency ($p = 0.11$), isolated wet extremes showed a marginally significant increasing tendency ($p = 0.08$), and dry-to-wet and wet-to-dry extremes showed a highly non-significant increasing tendency ($p > 0.45$). Both types of recurring extremes showed more dynamic patterns through time and were identified as having potential breakpoints. The dry-to-dry extreme was segmented into four periods—an increasing trend (1904–1933), followed by rapid increases in 1933 and 1951 with decreases until the next breakpoint (1933–1951, 1951–1969), followed by no trend from 1969 to 2022. The breakpoints in dry-to-dry extremes during the early 1930s and 1950s reflect severe regional droughts during this period (Putnam et al., 2008), and the decreasing trends during the windows reflects a return to normal conditions. In contrast, the wet-to-wet extreme time series had a single breakpoint in 2004. Prior to 2004, there was no significant trend. However, from 2004 to 2022, there was a substantial increase in the mean number of wet-to-wet extreme conditions relative to the prior period, indicating that there has been a potential step-change in the occurrence of wet-to-wet precipitation extremes in the region.

To inspect spatial patterns of extremes during each period, we normalized the total number of extremes during the period by the number of years in the period (fig. 11), representing the average number of extremes per year of that type during the interval. During the 1934–1951 period, which encompasses the Dust Bowl of the 1930s, dry-to-dry extreme occurrences were greatest in South Dakota and along the Kansas-Colorado-Texas-Oklahoma border. During the 1952–1969 period, dry-to-dry extremes were most common around the Kansas-Oklahoma border, Texas, and New Mexico. The periods 1905–1933 and 1970–2022 show relatively lower occurrence rates, with more frequent dry-to-dry events in the northern portion of the domain during recent years. For wet-to-wet extremes, the occurrence rate has increased substantially after 2004. Between 1905 and 2004, wet-to-wet extremes were more prevalent in Iowa, Montana, Oklahoma, Texas, Colorado, and New Mexico. However, after the step-change increase in wet-to-wet extremes (2005–2022), ocurrences were most frequent in Minnesota, Iowa, and Nebraska and along the North Dakota-South Dakota border, with relatively few occurrences in the Southern Great Plains.

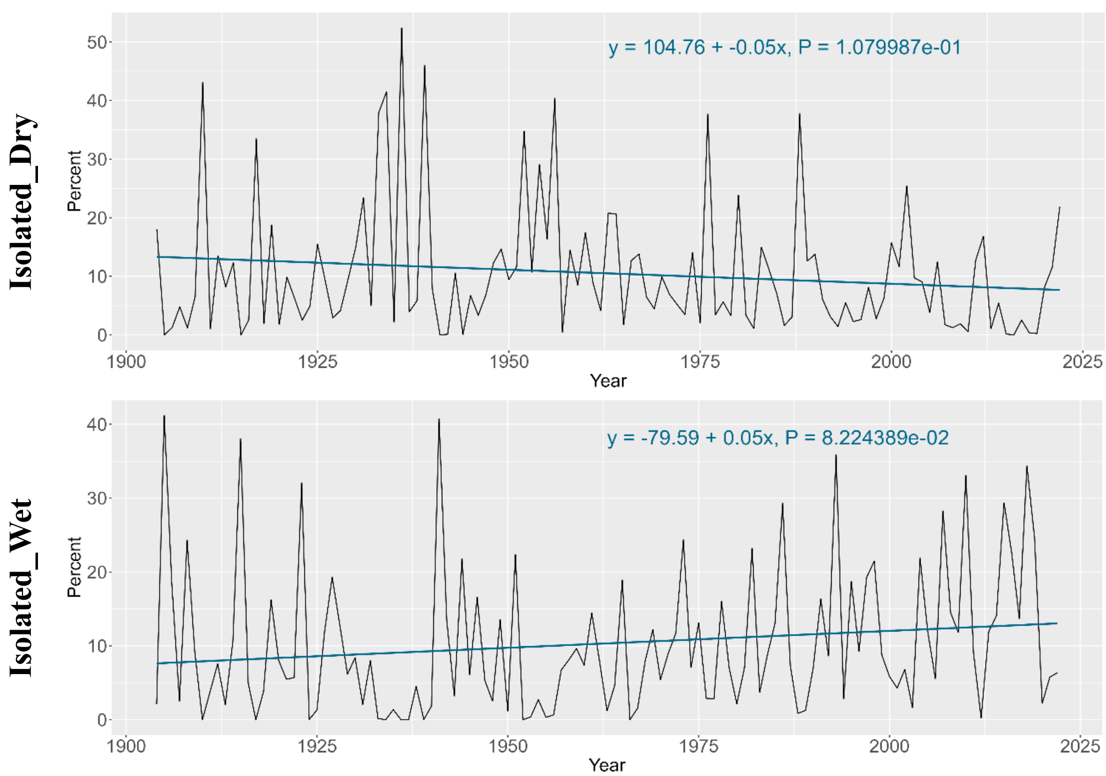

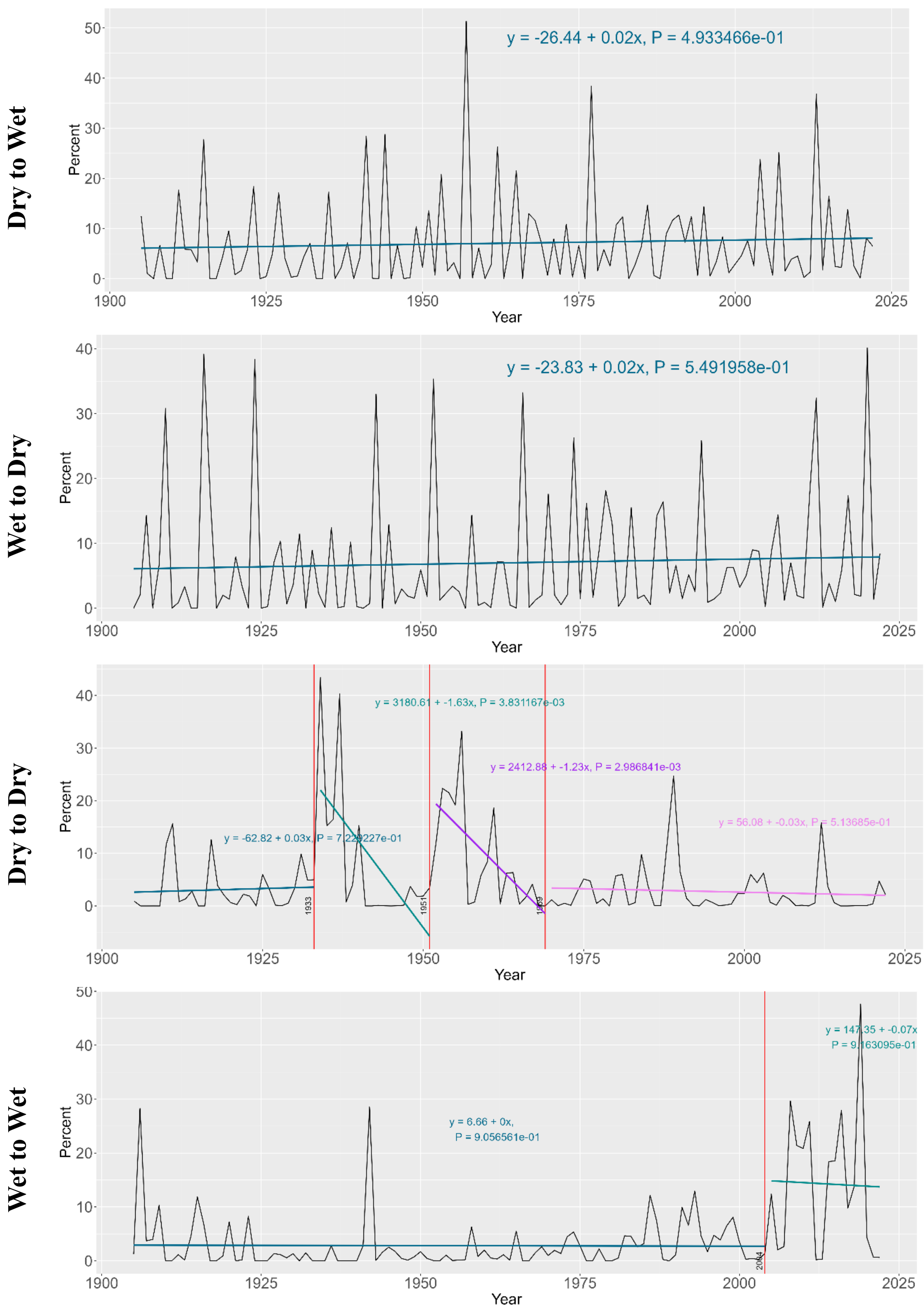

Figure 10. Percentage of USGP pixels experiencing each type of hydroclimatic extreme in each year. Vertical red lines show breakpoints where these were identified and blue and purple lines show trends within each period.

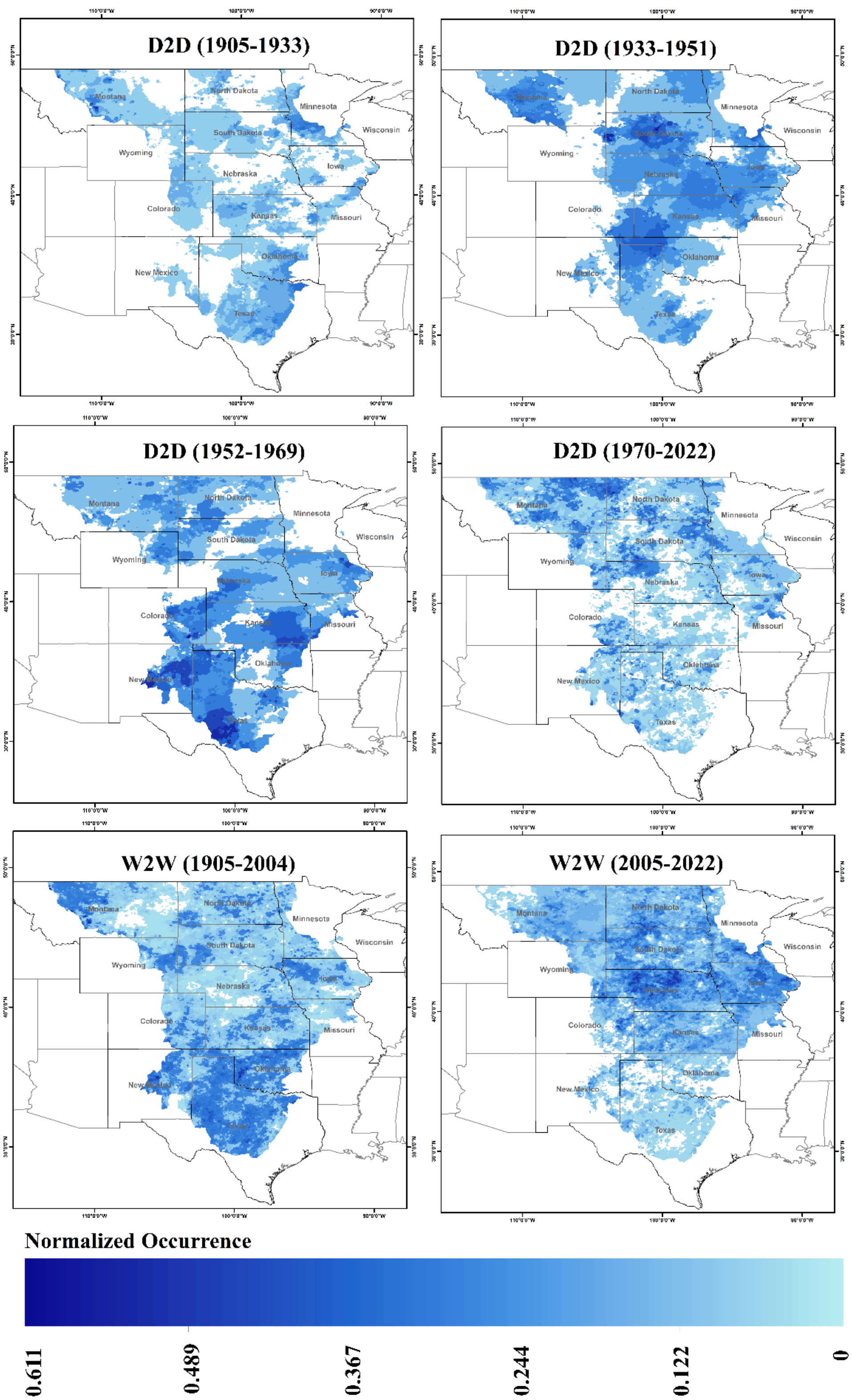

Figure 11. Maps of extremes per year for periods extracted from breakpoint analysis (fig. 10). D2D = dry-to-dry; W2W = wet-to-wet.

5. Conclusions

Changing hydroclimatic conditions in the USGP can affect water resources, agricultural systems, and society. Here, we analyzed changes in annual-scale precipitation and hydroclimatic extremes to provide insights into how the climate has changed and help inform best management practices in the water and agricultural sectors. To accomplish this, we addressed three objectives:

Objective 1: Assess the reliability of gridded PRISM data by comparing it to regional meteorological station-based data.

We found that PRISM data agreed well with station-based GHCND precipitation data at the annual resolution across our study area. For nearly all stations, the slope of the relationship between PRISM and GHCND was between 0.85 and 1.15 and $R^2 > 0.75$. Slopes were most commonly slightly over 1, suggesting that PRISM may slightly underestimate annual precipitation at the regional scale. This suggests that PRISM data provide a reasonable dataset for annual-scale analyses across the USGP, particularly using our percentile-based approach that identifies extremes based on the historical distribution of precipitation at each pixel.

Objective 2: Analyze long-term trends in annual precipitation across the USGP.

We found widespread significant increasing trends in annual precipitation across the wetter eastern portion of the USGP region and relatively few significant decreasing annual precipitation trends, which tended to be concentrated in the northwestern portion of the USGP. Broadly, this suggests that wetter regions of the USGP may also be experiencing increased annual precipitation. However, we are not able to comment on whether the region is broadly getting more or less arid, as we did not assess concurrent changes in potential ET or other metrics for the atmospheric demand for water.

Objective 3: Evaluate the spatial and temporal pattern of changing annual-scale precipitation extremes.

We assessed six types of annual-scale precipitation extremes: isolated wet and dry extremes, recurring wet-to-wet and dry-to-dry extremes, and whiplash dry-to-wet and wet-to-dry extremes. Frequent isolated wet occurrences were common in parts of Montana, North Dakota, Wyoming, and New Mexico, while isolated dry occurrences were more prevalent in Montana, Wyoming, North Dakota, South Dakota, Oklahoma, New Mexico, and Texas. Additionally, parts of Texas and Montana experienced more dry-to-dry extremes, while wet-to-wet extremes were observed more frequently in Iowa, parts of Nebraska, and South Dakota. Minnesota, Colorado, Oklahoma, and Texas experienced more dry-to-wet occurrences, while the central portion of the USGP—Kansas, Nebraska, Colorado, and North Texas—saw more wet-to-dry occurrences. Recurring extremes had the most dynamic time series through time, with spikes in dry-to-dry extremes during severe regional drought in the 1930s and 1950s and a potential step-change increase in wet-to-wet extremes over the past 20 years.

Overall, our analysis suggests that there is substantial spatial and temporal heterogeneity in historic annual-scale hydroclimatic extremes in the region. Future research priorities include identifying patterns and trends in seasonal extremes; quantifying concurrent changes in potential ET; and linking hydroclimatic extremes to impacts on reservoirs, water quality, agricultural productivity and water use, and other potential systems that are vulnerable to a changing climate.

References

Booth, E. G., Zipper, S. C., Loheide, S. P., and Kucharik, C. J., 2016, Is groundwater recharge always serving us well? Water supply provisioning, crop production, and flood attenuation in conflict in Wisconsin, USA: Ecosystem Services, v. 21, p. 153–165. https://doi.org/10.1016/j.ecoser.2016.08.007

Daly, C., Halbleib, M., Smith, J. I., Gibson, W. P., Doggett, M. K., Taylor, G. H., Curtis, J., and Pasteris, P., 2008, Physiographically sensitive mapping of climatological temperature and precipitation across the conterminous United States: International Journal of Climatology, v. 28, no. 15, p. 2,031–2,064. https://doi.org/10.1002/joc.1688

Facincani Dourado, G., Rheinheimer, D. E., Abaztoglou, J. T., and Viers, J. H., 2024, Stress testing California's hydroclimatic whiplash: Potential challenges, trade-offs and adaptations in water management and hydropower generation: Water Resources Research, v. 60, no. 7, e2023WR035966. https://doi.org/10.1029/2023WR035966

Hao, Z., Singh, V. P., and Hao, F., 2018, Compound extremes in hydroclimatology: A review: Water, v. 10, no. 6, p. 718. https://doi.org/10.3390/w10060718

Kaur, G., Singh, G., Motavalli, P. P., Nelson, K. A., Orlowski, J. M., and Golden, B. R., 2020, Impacts and management strategies for crop production in waterlogged or flooded soils: A review: Agronomy Journal, v. 112, no. 3, p. 1,475–1,501. https://doi.org/10.1002/agj2.20093

Lin, X., Harrington, J., Ciampitti, I., Gowda, P., Brown, D., and Kisekka, I., 2017, Kansas trends and changes in temperature, precipitation, drought, and frost-free days from the 1890s to 2015: Journal of Contemporary Water Research & Education, v. 162, no. 1, p. 18–30. https://doi.org/10.1111/j.1936-704X.2017.03257.x

Loecke, T. D., Burgin, A. J., Riveros-Iregui, D. A., Ward, A. S., Thomas, S. A., Davis, C. A., and Clair, M. A. S., 2017, Weather whiplash in agricultural regions drives deterioration of water quality: Biogeochemistry, 1–9. https://doi.org/10.1007/s10533-017-0315-z

Mourtzinis, S., Rattalino Edreira, J. I., Conley, S. P., and Grassini, P., 2017, From grid to field: Assessing quality of gridded weather data for agricultural applications: European Journal of Agronomy, v. 82, p. 163–172. https://doi.org/10.1016/j.eja.2016.10.013

Na, W., and Najafi, M. R., 2024, Rising risks of hydroclimatic swings: A large ensemble study of dry and wet spell transitions in North America: Global and Planetary Change, 238, 104476. https://doi.org/10.1016/j.gloplacha.2024.104476

Na, Y., Fu, Q., Leung, L. R., Kodama, C., and Lu, R., 2022, Mesoscale convective systems simulated by a high-resolution global nonhydrostatic model over the United States and China: Journal of Geophysical Research: Atmospheres, v. 127, no. 7, e2021JD035916. https://doi.org/10.1029/2021JD035916

PRISM Climate Group, 2024, PRISM Gridded Climate Data [Data set]. Retrieved from https://prism.oregonstate.edu

Putnam, J. E., Perry, C. A., and Wolock, D. M., 2008, Hydrologic droughts in Kansas: Are they becoming worse? (No. USGS Fact Sheet 2008-3034): US Geological Survey. Retrieved from https://pubs.usgs.gov/fs/2008/3034/

Schubert, S. D., Suarez, M. J., Pegion, P. J., Koster, R. D., and Bacmeister, J. T., 2004, Causes of long-term drought in the U.S. Great Plains: Journal of Climate, v. 17, no. 3. Retrieved from https://journals.ametsoc.org/view/journals/clim/17/3/1520-0442_2004_017_0485_coldit_2.0.co_2.xml

Seager, R., Feldman, J., Lis, N., Ting, M., Williams, A. P., Nakamura, J., Liu, H., and Henderson, N., 2017, Whither the 100th Meridian? The once and future physical and human geography of America's arid–humid divide; Part II: The meridian moves east: Earth Interactions, v. 22, no. 5, p. 1–24. https://doi.org/10.1175/EI-D-17-0012.1

Seager, R., Lis, N., Feldman, J., Ting, M., Williams, A. P., Nakamura, J., Liu, H., and Henderson, N., 2017, Whither the 100th Meridian? The once and future physical and human geography of America's arid–humid divide; Part I: The story so far: Earth Interactions, v. 22, no. 5, p. 1–22. https://doi.org/10.1175/EI-D-17-0011.1

Sillmann, J., Thorarinsdottir, T., Keenlyside, N., Schaller, N., Alexander, L. V., Hegerl, G., Seneviratne, S. I., Vautard, R., Zhang, X., and Zwiers, F. W., 2017, Understanding, modeling and predicting weather and climate extremes: Challenges and opportunities: Weather and Climate Extremes, v. 18, p. 65–74. https://doi.org/10.1016/j.wace.2017.10.003

Swain, D. L., Langenbrunner, B., Neelin, J. D., and Hall, A., 2018, Increasing precipitation volatility in twenty-first-century California: Nature Climate Change, v. 8, no. 5, p. 427–433. https://doi.org/10.1038/s41558-018-0140-y

Wang, S., Ancell, B., Yang, Z.-L., Duan, Q., and Anagnostou, E. N., 2022, Hydroclimatic extremes and impacts in a changing environment: Observations, mechanisms, and projections: Journal of Hydrology, v. 608, 127615. https://doi.org/10.1016/j.jhydrol.2022.127615

Whittemore, D. O., Butler, J. J., Bohling, G. C., and Wilson, B. B., 2023, Are we saving water? Simple methods for assessing the effectiveness of groundwater conservation measures: Agricultural Water Management, v. 287, 108408. https://doi.org/10.1016/j.agwat.2023.108408

Zipper, S. C., Farmer, W. H., Brookfield, A., Ajami, H., Reeves, H. W., Wardropper, C., Hammond, J. C., Gleeson, T., and Deines, J. M., 2022, Quantifying streamflow depletion from groundwater pumping: A practical review of past and emerging approaches for water management: JAWRA Journal of the American Water Resources Association, v. 58, no. 2, p. 289–312. https://doi.org/10.1111/1752-1688.12998

Zipper, S. C., Hammond, J. C., Shanafield, M., Zimmer, M., Datry, T., Jones, C. N., et al., 2021, Pervasive changes in stream intermittency across the United States: Environmental Research Letters, v. 16, no. 8, 084033. https://doi.org/10.1088/1748-9326/ac14ec

Zipper, S. C., Qiu, J., and Kucharik, C. J., 2016, Drought effects on US maize and soybean production: spatiotemporal patterns and historical changes: Environmental Research Letters, v. 11, no. 9, 094021. https://doi.org/10.1088/1748-9326/11/9/094021

Zipper, S. C., Soylu, M. E., Booth, E. G., and Loheide, S. P., 2015, Untangling the effects of shallow groundwater and soil texture as drivers of subfield-scale yield variability: Water Resources Research, v. 51, no. 8, p. 6,338–6,358. https://doi.org/10.1002/2015WR017522

Appendix

Table A1: List of the location-wise R^2 and slope values

GHCND Station	Latitude	Longitude	R^2	Equation	Slope
USC00051121	39.3062	-102.26085	0.85	y = 1.02 * x + -6.53	1.020
USC00053005	40.5763	-105.0857	0.89	y = 1.17 * x + -61.58	1.170
USC00054770	38.0936	-102.6306	0.90	y = 1.03 * x + 4.11	1.030
USC00054834	38.0635	-103.2152	0.84	y = 1.04 * x + -9.56	1.040
USC00054945	40.51461	-102.99068	0.83	y = 1.02 * x + 10.68	1.020
USC00057167	38.03846	-103.69477	0.89	y = 1.06 * x + -14.77	1.060
USC00059295	40.12367	-102.72171	0.78	y = 1 * x + 3.94	1.000
USC00130133	43.06626	-94.22216	0.87	y = 1.06 * x + -43.93	1.060
USC00130157	42.7536	-92.8022	0.90	y = 1.02 * x + -7.85	1.020
USC00130364	41.4175	-95.0041	0.82	y = 1 * x + -3.73	1.000
USC00130385	41.7069	-94.9222	0.91	y = 1.02 * x + -5.82	1.020
USC00130600	41.88136	-92.27642	0.90	y = 1.01 * x + 16.26	1.010
USC00130807	42.04167	-93.89088	0.96	y = 1.05 * x + -33.89	1.050
USC00131233	42.065	-94.85	0.90	y = 1.05 * x + -32.39	1.050
USC00131319	42.0496	-91.5881	0.91	y = 1.05 * x + -62.59	1.050
USC00131394	41.0163	-93.2791	0.94	y = 1.07 * x + -77.43	1.070
USC00131442	42.7572	-95.5377	0.94	y = 1.04 * x + -34.18	1.040
USC00131533	40.7242	-95.01918	0.93	y = 1.05 * x + -43.21	1.050
USC00131962	41.0372	-94.3936	0.88	y = 1.14 * x + -94.24	1.140
USC00132171	42.0363	-95.3288	0.93	y = 1.04 * x + -34.33	1.040
USC00132864	42.88262	-91.83025	0.92	y = 1.05 * x + -52.43	1.050
USC00132977	43.2844	-93.6305	0.88	y = 1.12 * x + -84.63	1.120
USC00132999	42.5836	-94.2005	0.84	y = 1 * x + 24.65	1.000
USC00133487	42.3647	-92.7594	0.82	y = 1.01 * x + 6.06	1.010
USC00134142	42.5188	-93.2536	0.91	y = 1.02 * x + -12.93	1.020
USC00134228	42.0103	-94.39523	0.93	y = 1.02 * x + -15.2	1.020
USC00134389	40.7468	-91.95745	0.84	y = 1.01 * x + -11.07	1.010
USC00134502	41.3247	-93.1008	0.78	y = 1.05 * x + -16.77	1.050
USC00134735	42.7816	-96.1458	0.86	y = 1.02 * x + 0.35	1.020
USC00134894	41.65	-95.806	0.92	y = 1.06 * x + -51.36	1.060
USC00135198	42.0647	-92.9244	0.94	y = 1.1 * x + -80.92	1.100
USC00135230	43.163	-93.1952	0.92	y = 1.04 * x + -37.26	1.040
USC00135769	40.7052	-94.2427	0.91	y = 1 * x + 9.68	1.000
USC00135796	40.96011	-91.5851	0.94	y = 1.01 * x + -0.63	1.010
USC00135952	43.0452	-92.3123	0.95	y = 1.13 * x + -118.44	1.130
USC00136151	41.3044	-95.3844	0.90	y = 1 * x + -3.44	1.000
USC00136327	41.3213	-92.6466	0.80	y = 1.12 * x + -109.16	1.120
USC00136566	41.8394	-94.1105	0.92	y = 1.08 * x + -54.32	1.080

GHCND Station	Latitude	Longitude	R^2	Equation	Slope
USC00136719	42.7291	-94.6613	0.93	y = 1.01 * x + -9.88	1.010
USC00137161	42.3969	-94.6291	0.91	y = 1.07 * x + -42.53	1.070
USC00137312	42.4194	-94.9761	0.93	y = 1.08 * x + -76.48	1.080
USC00137386	43.1791	-95.6602	0.92	y = 1.03 * x + -8.03	1.030
USC00137678	41.3371	-92.2279	0.95	y = 1.06 * x + -58.76	1.060
USC00138296	42.03543	-92.58046	0.90	y = 1.09 * x + -40.83	1.090
USC00138490	41.5338	-93.9502	0.91	y = 1.05 * x + -46.26	1.050
USC00138688	41.2825	-91.7078	0.94	y = 1.04 * x + -27.3	1.040
USC00140365	37.1941	-99.7632	0.85	y = 0.99 * x + 2.53	0.990
USC00140405	39.5755	-95.1108	0.94	y = 1.02 * x + -15.24	1.020
USC00140439	39.79957	-101.04213	0.93	y = 1.06 * x + -26.05	1.060
USC00140911	39.677	-96.663	0.94	y = 1.02 * x + -26.96	1.020
USC00141522	37.8133	-100.3456	0.86	y = 1.07 * x + -23.09	1.070
USC00141559	39.3739	-97.1274	0.92	y = 1.04 * x + -21.11	1.040
USC00141740	37.16806	-94.83002	0.95	y = 1.02 * x + -28.93	1.020
USC00141858	38.3703	-96.5483	0.95	y = 1.03 * x + -37.03	1.030
USC00142213	39.62523	-100.42339	0.93	y = 1.12 * x + -55.99	1.120
USC00142835	37.81718	-94.69872	0.94	y = 1.01 * x + -15.76	1.010
USC00142894	37.534	-95.827	0.93	y = 1 * x + -18.58	1.000
USC00143008	38.28	-95.2177	0.93	y = 1.01 * x + 3.39	1.010
USC00143239	37.60255	-99.30224	0.82	y = 0.99 * x + 0.58	0.990
USC00143527	38.8586	-99.3358	0.89	y = 0.97 * x + 18.61	0.970
USC00143554	38.6002	-100.6196	0.93	y = 1.1 * x + -50.88	1.100
USC00143594	38.66533	-96.94925	0.95	y = 1.04 * x + -35.39	1.040
USC00143810	39.6679	-95.5199	0.94	y = 1.03 * x + -37.58	1.030
USC00143837	39.35698	-100.44179	0.91	y = 1.06 * x + -24.65	1.060
USC00143847	38.1041	-98.6592	0.93	y = 1.01 * x + -6.13	1.010
USC00143855	37.1639	-101.3401	0.86	y = 1.11 * x + -39.91	1.110
USC00143954	37.2363	-95.7002	0.93	y = 1.02 * x + -23.35	1.020
USC00143984	37.9233	-95.4241	0.97	y = 1.02 * x + -42.99	1.020
USC00144464	37.9412	-101.2492	0.81	y = 1.08 * x + -31.25	1.080
USC00144675	38.08	-95.6396	0.93	y = 1.02 * x + -33.53	1.020
USC00144695	37.0309	-100.9069	0.90	y = 1.04 * x + -7.28	1.040
USC00144712	39.0294	-98.13	0.91	y = 1.09 * x + -62.38	1.090
USC00144972	39.1972	-96.5813	0.95	y = 1.07 * x + -39.27	1.070
USC00145132	39.05391	-96.23658	0.94	y = 1.05 * x + -41.82	1.050
USC00145152	38.3772	-97.6097	0.92	y = 1.01 * x + -12.44	1.010
USC00145363	39.1246	-97.7047	0.95	y = 1.03 * x + -28.35	1.030
USC00145539	37.8658	-97.6648	0.95	y = 1.04 * x + -24.98	1.040
USC00145744	38.0231	-97.35525	0.90	y = 1.04 * x + -13.29	1.040
USC00145888	39.11298	-100.9447	0.91	y = 1.04 * x + 1.11	1.040

GHCND Station	Latitude	Longitude	R^2	Equation	Slope
USC00145906	39.8229	-100.5163	0.90	y = 1.05 * x + -28.24	1.050
USC00146128	38.6132	-95.2808	0.94	y = 1.02 * x + -10.03	1.020
USC00146435	39.245	-99.3808	0.92	y = 1.05 * x + -18.72	1.050
USC00146549	37.67313	-98.77621	0.88	y = 1.01 * x + -2.7	1.010
USC00147093	39.7675	-101.8066	0.91	y = 1.05 * x + -11.43	1.050
USC00147305	37.1322	-96.18	0.92	y = 1.02 * x + -3.39	1.020
USC00147542	39.7772	-98.7783	0.92	y = 1.03 * x + -23.69	1.030
USC00148038	37.9929	-101.7417	0.81	y = 1.06 * x + -14.54	1.060
USC00148549	37.54397	-95.04761	0.90	y = 0.99 * x + -5.31	0.990
USC00148563	39.21418	-96.37005	0.93	y = 1.04 * x + -21.62	1.040
USC00148964	37.28851	-96.94076	0.90	y = 1.07 * x + -65.49	1.070
USC00210075	43.6064	-93.3019	0.90	y = 1.1 * x + -87.67	1.100
USC00210287	45.38564	-96.12578	0.91	y = 1.11 * x + -67.5	1.110
USC00211891	47.8186	-96.6139	0.85	y = 1 * x + 1.09	1.000
USC00213290	43.7047	-92.5644	0.93	y = 1.06 * x + -41.92	1.060
USC00215400	45.1219	-95.9269	0.94	y = 1.09 * x + -42.44	1.090
USC00215638	45.5901	-95.8745	0.92	y = 1.02 * x + -4.26	1.020
USC00216565	44.0138	-96.3258	0.89	y = 0.99 * x + 9.61	0.990
USC00216787	47.87945	-96.28446	0.88	y = 1.08 * x + -39.34	1.080
USC00218323	44.2394	-95.6308	0.86	y = 1.05 * x + -40.04	1.050
USC00218692	44.07063	-93.52647	0.92	y = 1.05 * x + -32.37	1.050
USC00218907	45.80808	-96.50419	0.86	y = 1.02 * x + -6.88	1.020
USC00219046	43.7639	-94.1662	0.95	y = 1.03 * x + -24.76	1.030
USC00230204	38.18945	-94.0244	0.94	y = 1.05 * x + -61.76	1.050
USC00230608	40.2575	-94.0269	0.86	y = 0.98 * x + 5.72	0.980
USC00231580	39.775	-93.5357	0.94	y = 1.02 * x + -59.53	1.020
USC00231711	38.395	-93.7711	0.90	y = 1 * x + -15.9	1.000
USC00231822	40.2394	-94.6833	0.92	y = 1.07 * x + -54.33	1.070
USC00234705	37.5984	-94.2842	0.86	y = 1.06 * x + -58.03	1.060
USC00235340	40.3458	-94.8341	0.92	y = 1.03 * x + -24.63	1.030
USC00235987	37.8395	-94.374	0.95	y = 1 * x + -28.71	1.000
USC00238051	39.97018	-91.88753	0.89	y = 1.02 * x + -2.71	1.020
USC00240364	47.4926	-112.397	0.89	y = 1.16 * x + -57.54	1.160
USC00240770	48.13514	-110.06364	0.82	y = 1.04 * x + -12.66	1.040
USC00241102	45.3261	-108.9091	0.13	y = 1.08 * x + -13.24	1.080
USC00242122	48.14739	-104.51745	0.94	y = 1.06 * x + -20.53	1.060
USC00242689	45.8863	-104.5478	0.93	y = 1.05 * x + -29.68	1.050
USC00243013	46.82169	-108.37239	0.92	y = 1.01 * x + -10.48	1.010
USC00243110	48.4982	-109.8014	0.93	y = 1.05 * x + -17.04	1.050
USC00243581	47.1059	-104.71759	0.86	y = 1 * x + 7.5	1.000
USC00244241	46.9907	-112.0116	0.92	y = 1.07 * x + -36.16	1.070

GHCND Station	Latitude	Longitude	R^2	Equation	Slope
USC00244345	45.9227	-108.2453	0.93	y = 1.07 * x + -24.08	1.070
USC00246601	46.4177	-104.5163	0.92	y = 1.04 * x + -15.88	1.040
USC00246918	45.1769	-109.2571	0.81	y = 1.15 * x + -72.13	1.150
USC00250050	42.54669	-99.85161	0.90	y = 1.08 * x + -33.9	1.080
USC00250320	41.4266	-99.1272	0.94	y = 1.04 * x + -29.02	1.040
USC00250435	40.3705	-95.7469	0.83	y = 1.05 * x + -2.33	1.050
USC00250640	40.1305	-99.8277	0.92	y = 1 * x + 0.28	1.000
USC00251065	40.87948	-97.75071	0.86	y = 1.12 * x + -74.6	1.120
USC00251200	41.4083	-99.675	0.93	y = 1.01 * x + 0.26	1.010
USC00251365	42.913	-98.8511	0.95	y = 1.05 * x + -25.45	1.050
USC00251575	42.8083	-103.0533	0.84	y = 1.08 * x + -45.34	1.080
USC00251680	40.5033	-97.9372	0.92	y = 1.08 * x + -64.14	1.080
USC00251825	41.4638	-97.3277	0.93	y = 1.03 * x + -30.61	1.030
USC00252020	40.6092	-96.872	0.91	y = 1.03 * x + -9.81	1.030
USC00252065	40.23154	-100.83026	0.94	y = 1.02 * x + -12.49	1.020
USC00252595	41.9872	-98.0747	0.87	y = 0.97 * x + 24.19	0.970
USC00252690	40.4767	-99.8861	0.92	y = 1.05 * x + -27.28	1.050
USC00252770	41.8036	-98.8239	0.82	y = 0.94 * x + 9.79	0.940
USC00252820	40.0738	-97.1669	0.93	y = 1.05 * x + -27.51	1.050
USC00253050	41.43	-96.4669	0.93	y = 1.05 * x + -25.29	1.050
USC00253175	40.53936	-97.59048	0.88	y = 1.03 * x + -2.38	1.030
USC00253185	41.4513	-97.7644	0.91	y = 0.99 * x + 2.14	0.990
USC00253365	40.9394	-100.1513	0.95	y = 1.01 * x + -15.65	1.010
USC00253605	41.633	-103.9541	0.90	y = 1.07 * x + -35.79	1.070
USC00253615	42.6858	-103.8841	0.90	y = 1.09 * x + -9.58	1.090
USC00253630	42.61664	-97.2608	0.92	y = 1.03 * x + -12.72	1.030
USC00253660	40.6471	-98.3835	0.88	y = 1.01 * x + -7.11	1.010
USC00253735	40.175	-97.5902	0.93	y = 1.02 * x + -22.91	1.020
USC00253910	40.4518	-99.3802	0.91	y = 1.04 * x + -15.91	1.040
USC00254110	40.50905	-101.65147	0.85	y = 1.03 * x + 5.77	1.030
USC00254335	40.7258	-99.0133	0.94	y = 1.07 * x + -42.93	1.070
USC00254985	41.2789	-98.9697	0.92	y = 1.05 * x + -34.36	1.050
USC00255090	40.8508	-101.5427	0.75	y = 0.98 * x + 21.37	0.980
USC00255310	40.22887	-100.61	0.86	y = 1.04 * x + -12.89	1.040
USC00255525	40.9283	-99.3886	0.88	y = 1.03 * x + -17.39	1.030
USC00255565	40.5155	-98.9513	0.86	y = 1.03 * x + -11.02	1.030
USC00256135	42.067	-97.9653	0.94	y = 1.03 * x + -15.6	1.030
USC00256385	41.4014	-102.3465	0.93	y = 1.02 * x + -17.17	1.020
USC00256970	42.065	-100.2472	0.69	y = 1.04 * x + 0.44	1.040
USC00257040	41.0319	-98.9213	0.79	y = 1.12 * x + -65.7	1.120
USC00257070	40.0977	-98.5197	0.94	y = 1 * x + -1.12	1.000

GHCND Station	Latitude	Longitude	R^2	Equation	Slope
USC00257515	41.2077	-98.4608	0.92	y = 0.96 * x + 25.91	0.960
USC00257715	40.9169	-97.0898	0.88	y = 1.01 * x + 9.65	1.010
USC00257830	41.2294	-103.0214	0.83	y = 1.06 * x + -24.89	1.060
USC00258395	40.6661	-96.1891	0.94	y = 1.01 * x + -5.95	1.010
USC00258410	40.2381	-96.0847	0.95	y = 1.04 * x + -36.29	1.040
USC00258480	41.788	-96.2326	0.92	y = 1.06 * x + -41.35	1.060
USC00258745	40.8972	-97.3463	0.90	y = 1.03 * x + -20.56	1.030
USC00258915	42.30168	-96.90022	0.92	y = 1.05 * x + -27.22	1.050
USC00259200	41.845	-96.7141	0.93	y = 1.03 * x + -14.92	1.030
USC00296619	36.2994	-103.7408	0.85	y = 1.11 * x + -49.32	1.110
USC00299156	35.2005	-103.6866	0.93	y = 1.04 * x + -21.38	1.040
USC00320995	46.19361	-103.37138	0.82	y = 1.04 * x + -10.9	1.040
USC00321871	48.91583	-103.29805	0.92	y = 1.05 * x + -14.87	1.050
USC00323287	46.15833	-98.39888	0.91	y = 1.09 * x + -11.7	1.090
USC00323621	47.92172	-97.0975	0.86	y = 1.01 * x + 1.89	1.010
USC00324418	46.8844	-98.685	0.87	y = 1.11 * x + -40.32	1.110
USC00324958	48.7622	-98.3447	0.86	y = 1.02 * x + -6.29	1.020
USC00325479	46.8127	-100.9097	0.82	y = 0.9 * x + 28.31	0.900
USC00325710	47.48277	-100.445	0.56	y = 0.88 * x + 79.22	0.880
USC00325754	46.3911	-97.2391	0.88	y = 1.04 * x + -18.42	1.040
USC00325993	48.1802	-101.2963	0.95	y = 1.08 * x + -36.76	1.080
USC00326025	48.7602	-101.509	0.79	y = 1.13 * x + -37.48	1.130
USC00326255	46.51111	-99.7725	0.89	y = 0.99 * x + 4.67	0.990
USC00326315	46.54055	-102.86916	0.85	y = 1.04 * x + -6.96	1.040
USC00326365	46.8925	-101.4897	0.92	y = 1.04 * x + -12.84	1.040
USC00327530	46.8886	-102.3191	0.86	y = 1.06 * x + -18.15	1.060
USC00328840	47.5213	-100.8883	0.63	y = 0.97 * x + 28.61	0.970
USC00329445	48.606	-100.291	0.90	y = 1.06 * x + -25.4	1.060
USC00340292	34.1773	-97.1617	0.91	y = 1.05 * x + -28.12	1.050
USC00342912	36.4194	-97.8747	0.88	y = 1.04 * x + -38.74	1.040
USC00343497	35.6306	-98.3217	0.90	y = 1.02 * x + -10.88	1.020
USC00344573	36.68562	-97.74861	0.75	y = 1.15 * x + -98.38	1.150
USC00344861	35.8582	-97.9295	0.94	y = 1.06 * x + -58.76	1.060
USC00345063	34.6098	-98.4573	0.89	y = 1.05 * x + -26.72	1.050
USC00345581	34.6368	-97.9786	0.95	y = 1.04 * x + -42.15	1.040
USC00346278	36.94227	-97.00586	0.88	y = 1.05 * x + -46.41	1.050
USC00348110	35.3552	-96.92031	0.93	y = 1.05 * x + -33.14	1.050
USC00348501	36.1175	-97.095	0.88	y = 1.02 * x + -20.89	1.020
USC00348884	34.20695	-96.64242	0.92	y = 1.06 * x + -77.79	1.060
USC00349422	35.5199	-98.6986	0.88	y = 1.03 * x + 1.14	1.030
USC00349760	36.4408	-99.3819	0.84	y = 1.05 * x + -2.8	1.050

GHCND Station	Latitude	Longitude	R^2	Equation	Slope
USC00390043	43.48944	-99.06289	0.93	y = 1.07 * x + -36.65	1.070
USC00390128	43.65133	-97.79811	0.91	y = 1.01 * x + -13	1.010
USC00391049	45.78861	-97.74881	0.94	y = 1.06 * x + -46.19	1.060
USC00391076	44.32503	-96.76864	0.90	y = 1.01 * x + -31.46	1.010
USC00391294	45.5488	-103.9744	0.90	y = 0.99 * x + -3.49	0.990
USC00391392	43.3111	-96.5878	0.92	y = 0.98 * x + 19.41	0.980
USC00391972	43.9611	-101.8605	0.85	y = 1.02 * x + -7.89	1.020
USC00392087	43.7744	-103.6119	0.69	y = 1.13 * x + -49.91	1.130
USC00392429	45.04689	-101.60228	0.92	y = 1.05 * x + -26.21	1.050
USC00392797	45.76542	-99.6222	0.91	y = 1.02 * x + -12.75	1.020
USC00392927	45.03239	-99.12253	0.94	y = 1.06 * x + -28.21	1.060
USC00392984	44.05162	-96.5927	0.93	y = 1.02 * x + -25.97	1.020
USC00393029	44.06844	-98.08333	0.89	y = 1.03 * x + -11.54	1.030
USC00393832	44.51376	-99.44211	0.81	y = 1.04 * x + -22.03	1.040
USC00394516	43.90239	-99.85815	0.95	y = 1.04 * x + -14.5	1.040
USC00394834	44.3544	-103.7431	0.92	y = 1.03 * x + -25.53	1.030
USC00395228	43.42089	-97.25389	0.89	y = 1.01 * x + 5.06	1.010
USC00395381	45.83825	-101.27683	0.80	y = 0.94 * x + 34.62	0.940
USC00395481	43.23586	-97.57125	0.87	y = 0.99 * x + 18.95	0.990
USC00395561	44.5177	-98.98148	0.87	y = 1.07 * x + -28.42	1.070
USC00395891	43.8878	-100.7075	0.84	y = 1.09 * x + -31.24	1.090
USC00396054	44.71371	-103.42584	0.87	y = 0.98 * x + 5.19	0.980
USC00396292	44.73234	-100.14479	0.92	y = 1.06 * x + -37.74	1.060
USC00396712	45.90338	-100.28765	0.93	y = 1.01 * x + -5.92	1.010
USC00397882	44.49739	-103.87177	0.82	y = 1.08 * x + -29.03	1.080
USC00398472	42.99179	-97.87022	0.85	y = 0.98 * x + 25.78	0.980
USC00398622	42.7625	-96.9194	0.89	y = 1.09 * x + -60.21	1.090
USC00399232	43.68724	-98.67155	0.85	y = 0.99 * x + 8.62	0.990
USC00399442	43.4989	-100.4814	0.90	y = 1.04 * x + -12.98	1.040
USC00410120	32.7047	-99.3012	0.89	y = 1.01 * x + 0.05	1.010
USC00410394	33.15251	-100.23319	0.93	y = 1.05 * x + -22.9	1.050
USC00410493	31.7413	-99.9763	0.84	y = 1.06 * x + -35.4	1.060
USC00410902	29.7986	-98.7353	0.95	y = 1.05 * x + -48.88	1.050
USC00411138	31.72278	-99.01417	0.89	y = 1.04 * x + -35.97	1.040
USC00411875	31.82795	-99.41777	0.90	y = 1.05 * x + -23.25	1.050
USC00412121	33.66078	-101.27774	0.87	y = 1.04 * x + -7.82	1.040
USC00412142	33.9898	-99.73024	0.85	y = 1.08 * x + -47.51	1.080
USC00412404	33.1991	-97.1049	0.94	y = 1.06 * x + -64.92	1.060
USC00414182	32.0161	-97.1094	0.93	y = 1.04 * x + -23.74	1.040
USC00415272	30.7426	-98.6543	0.89	y = 1.08 * x + -48.51	1.080
USC00415821	34.72611	-100.53722	0.88	y = 1 * x + 4.06	1.000

GHCND Station	Latitude	Longitude	R^2	Equation	Slope
USC00477226	44.8544	-92.6122	0.92	y = 1.08 * x + -45.46	1.080
USW00013980	37.155	-98.0282	0.91	y = 1.01 * x + -16.25	1.010
USW00013985	37.77105	-99.96915	0.90	y = 1 * x + -1.38	1.000
USW00014924	48.9713	-97.2414	0.63	y = 0.97 * x + 18.46	0.970
USW00014929	45.44358	-98.41384	0.82	y = 1.16 * x + -55.77	1.160
USW00014936	44.37916	-98.22275	0.94	y = 1.06 * x + -44.59	1.060
USW00014946	44.90452	-97.14957	0.79	y = 0.95 * x + 22.9	0.950
USW00023065	39.36729	-101.69322	0.85	y = 1 * x + -1.07	1.000
USW00024020	40.52315	-101.03456	0.81	y = 1.03 * x + 16.81	1.030
USW00024028	41.87466	-103.60112	0.83	y = 1.05 * x + -10.06	1.050
USW00024036	47.05443	-109.45654	0.77	y = 1.02 * x + -0.28	1.020
USW00024137	48.60355	-112.37663	0.77	y = 1.07 * x + -24.79	1.070
USW00093986	34.98908	-99.05282	0.82	y = 0.95 * x + 12.31	0.950
USW00094957	40.07912	-95.58928	0.86	y = 1.05 * x + -22.92	1.050

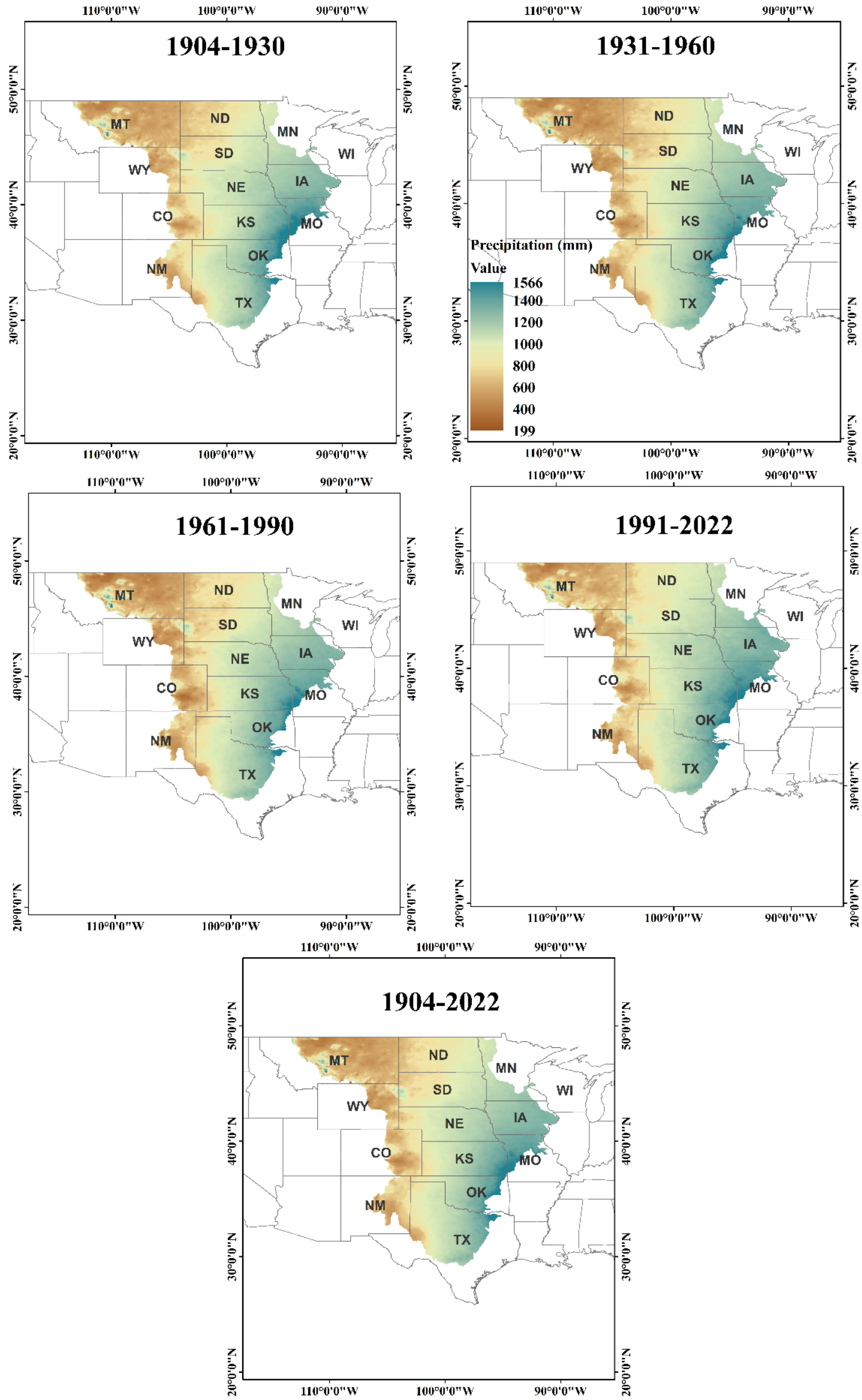

Figure A1. Average annual rainfall for each 30-year interval and the entire 1904–2022 period.

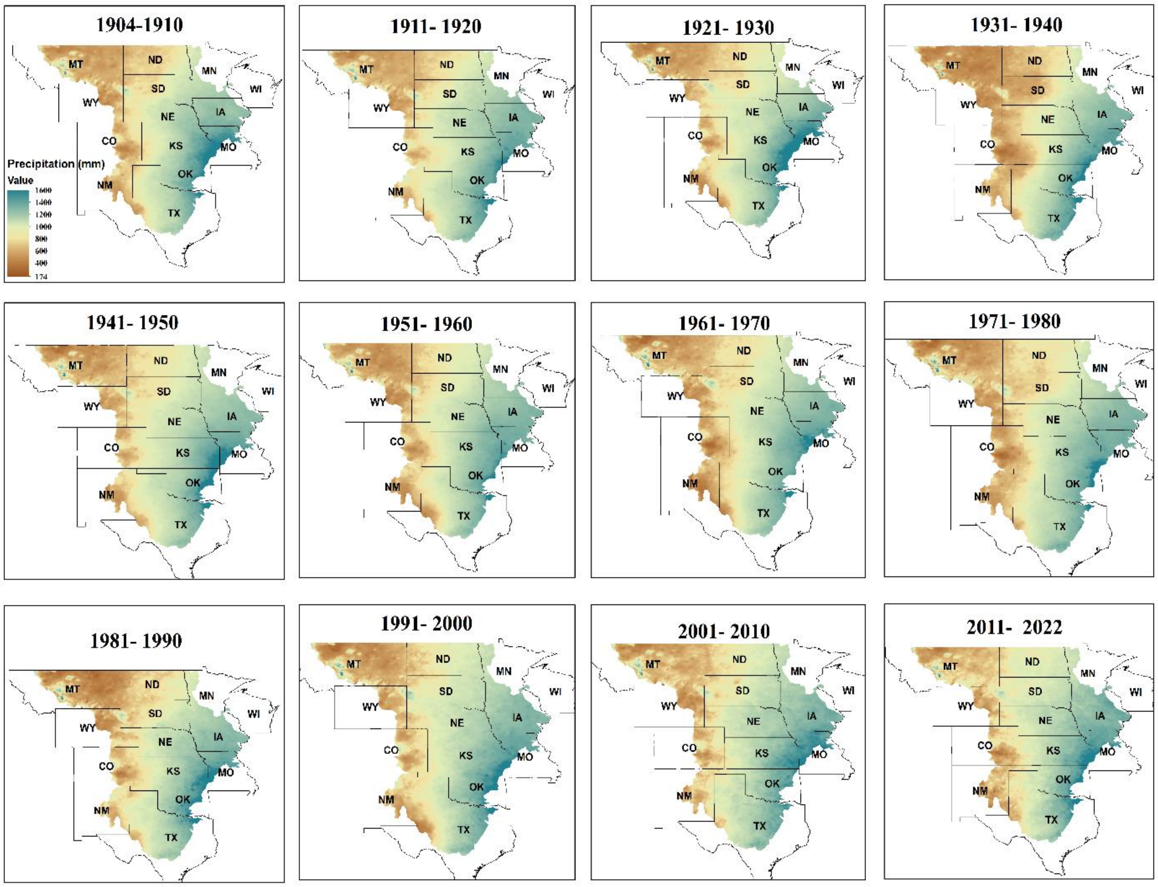

Figure A2. Average annual rainfall for each 10-year interval during the study period.

Supplemental Info: Code used in analyses

R code for percentile rank calculation

```r
############ Percentile rank Calculation ########################

input_folder <- "D:/KGS/PRISM/extreme_events_occurrance_files/3rd_attempt_Texas2/1_annual_precipitation_Texas2_layer"
output_folder <- "D:/KGS/PRISM/extreme_events_occurrance_files/3rd_attempt_Texas2/2_Annual_Percentile_Rank"
raster_files <- list.files(input_folder, pattern = "\\.tif$", full.names = TRUE) #stored in vector

# custom function to calculate percentile ranks for all rasters
calculate_percentile_ranks <- function(raster_files) {
  raster_collection <- rast(raster_files)      #raster files in single raster collection
  pixel_values <- values(raster_collection)  #extract pixel value in matrix

  ranks <- apply(pixel_values, 1, function(x) {     #row by row= pixel value
    valid_x <- x[!is.na(x)]  # remove NA value from pixel (did this because it showed error, assuming because of NA value near edge)
    if (length(valid_x) > 0) {  #if non-NA >0
      # ranking
      ranks <- rank(valid_x)
      # calculating percentile
      percentile_ranks <- round((ranks - 0.5) / length(valid_x) * 100, 2)
      # creating vector with NA
      rank_result <- rep(NA, length(x))
      # replacing the NA with percentile rank
      rank_result[!is.na(x)] <- percentile_ranks
      return(rank_result) # gives non-NA
    } else {
      return(rep(NA, length(x))) #put NA value if no non_NA
    }
  })

  ranks <- t(ranks) #pixel-raster to raster-pixel #setValues() function need this format

  result_rasters <- rast(raster_collection)   # taking the raster collections
  for (i in 1:ncol(ranks)) {    # each column of t matrix (raster) to value
    result_rasters[[i]] <- setValues(result_rasters[[i]], ranks[, i]) # set value i-th raster (raster object), i-th pixel value (numeric)
  }

  return(result_rasters)
}

# Calculate percentile rank rasters for all rasters
percentile_rasters <- calculate_percentile_ranks(raster_files)
```

R code for percentile rank change calculation

```r
########### Percentile Change ##############

input_folder <- "D:/KGS/PRISM/extreme_events_occurrance_files/3rd_attempt_Texas2/2_Annual_Percentile_Rank"
file_names <- list.files(path = input_folder, pattern = "*.tif", full.names = TRUE)
percentile_rasters <- lapply(file_names, raster)

# Calculate percentile rank change between consecutive years
change_rasters <- list()
for (i in 1:(length(percentile_rasters) - 1)) {
  change_raster <- percentile_rasters[[i]] - percentile_rasters[[i+1]]

  # Extract year from file name #did not work
  year1 <- gsub(".*_(\\d{4})\\.tif", "\\1", basename(file_names[i]))
  year2 <- gsub(".*_(\\d{4})\\.tif", "\\1", basename(file_names[i+1]))

  folder_path <- "D:/KGS/PRISM/extreme_events_occurrance_files/3rd_attempt_Texas2/3_Annual_Percentile_Rank_Change"
  file_name <- paste0("percentile_rank_change_", year1, "_", year2, ".tif")

  # Save the raster to a file
  writeRaster(change_raster, file.path(folder_path, file_name), overwrite=TRUE)

  # Add the change raster to the list
  change_rasters <- c(change_rasters, list(change_raster))
}


# Renaming

input_folder <- "D:/KGS/PRISM/extreme_events_occurrance_files/3rd_attempt_Texas2/3_Annual_Percentile_Rank_Change"
output_folder <- "D:/KGS/PRISM/extreme_events_occurrance_files/3rd_attempt_Texas2/4_Annual_Percentile_Rank_Change_renamed"
file_names <- list.files(path = input_folder, pattern = "*.tif", full.names = TRUE)

# Rename the files
for (i in 1:length(file_names)) {
  old_name <- file_names[i]
  file_name <- basename(old_name)
  year1 <- gsub(".*_rank_change_percentile_rank_PRISM_total_annual_rainfall_(\\d{4})_.*\\.tif", "\\1", file_name)
  year2 <- gsub(".*_rank_PRISM_total_annual_rainfall_(\\d{4})_.*$", "\\1", gsub("^.+_(\\d{4})_.*\\.tif\\.tif", "\\1", file_name))
  new_name <- paste0("percentile_rank_change_", year1, "_", year2, ".tif")
  file.copy(from = old_name, to = file.path(output_folder, new_name))
}
```

R code for percentile rank change conditions

```r
############## Condition ###################
# is_wet = percentile_precipitation >= 80,
# is_dry = percentile_precipitation <= 20,
# is_wet2dry = percentile_change >= 60,
# is_dry2wet = percentile_change <= -60,
# wet2wet = is_wet & lag(is_wet),
# dry2dry = is_dry & lag(is_dry)


############## Isolated Wet (percentile_precipitation >= 80) ##############

input_folder <- "D:/KGS/PRISM/extreme_events_occurrance_files/3rd_attempt_Texas2/2_Annual_Percentile_Rank"
output_folder <- "D:/KGS/PRISM/extreme_events_occurrance_files/3rd_attempt_Texas2/5_Annual_Percentile_Rank_Change_renamed_Is_Wet"
file_names <- list.files(path = input_folder, pattern = "*.tif", full.names = TRUE)

# Loop through each file and create a new raster
for (i in 1:length(file_names)) {
  # Read the original raster
  r <- raster(file_names[i])

  # Create a new raster with the same extent, resolution, and CRS as the original
  new_r <- r

  # Assign the new values to the raster
  values(new_r) <- ifelse(values(r) >= 80, 1, 0)

  # Write the new raster to a file
  writeRaster(new_r, filename = file.path(output_folder, paste0("event_", basename(file_names[i]))),
              format = "GTiff", datatype = "INT1U", overwrite = TRUE)
}

# stacking and sum
input_folder <- "D:/KGS/PRISM/extreme_events_occurrance_files/3rd_attempt_Texas2/5_Annual_Percentile_Rank_Change_renamed_Is_Wet"
output_folder <- "D:/KGS/PRISM/extreme_events_occurrance_files/3rd_attempt_Texas2/5_Annual_Percentile_Rank_Change_renamed_Is_Wet/event_is_wet"
output_filename <- "Event_count_Is_Wet_1904_2022.tif"

raster_files <- list.files(input_folder, pattern = "\\.tif$", full.names = TRUE)
raster_stack <- stack(raster_files)
summed_raster <- calc(raster_stack, sum, na.rm = TRUE)

output_file <- file.path(output_folder, output_filename)
writeRaster(summed_raster, output_file, format = "GTiff", overwrite = TRUE)
```

R code for ensuring only one true value per year based on priority

```r
########### Ensure only one TRUE value per year based on priority #############
# created from previous layers #
input_folder <- "D:/KGS/PRISM/extreme_events_occurrance_files/3rd_attempt_Wyoming/Input"
output_folder <- "D:/KGS/PRISM/extreme_events_occurrance_files/3rd_attempt_Wyoming/Output"
folders <- c("Is_Wet", "Is_Dry", "W2D", "D2W", "W2W", "D2D")

# an empty list to store the rasters
rasters <- list()

# Loop and read in the rasters
for (folder in folders) {
  folder_path <- file.path(input_folder, folder)
  rasters[[folder]] <- list.files(folder_path, pattern = "*.tif", full.names = TRUE) %>%
    lapply(raster)
}

# Find the minimum number of rasters across all folders
min_rasters <- min(sapply(rasters, length))
# Loop through each year
for (i in 1:min_rasters) {
  # Extract the rasters for each year
  is_wet <- rasters[["Is_Wet"]][[i]]
  is_dry <- rasters[["Is_Dry"]][[i]]
  w2d <- rasters[["W2D"]][[i]]
  d2w <- rasters[["D2W"]][[i]]
  w2w <- rasters[["W2W"]][[i]]
  d2d <- rasters[["D2D"]][[i]]

  # Perform the operations
  is_wet2dry <- ifelse(is.na(w2d[]), 0, w2d[])
  is_dry2wet <- ifelse(is.na(d2w[]), 0, d2w[])
  wet2wet <- ifelse(is.na(w2w[]), 0, w2w[])
  dry2dry <- ifelse(is.na(d2d[]), 0, d2d[])
  is_wet_new <- ifelse(is.na(is_wet[]), 0, is_wet[])
  is_dry_new <- ifelse(is.na(is_dry[]), 0, is_dry[])

  is_wet2dry <- ifelse(is_wet2dry == 1, 1, 0)
  is_dry2wet <- ifelse((is_wet2dry == 0) & (is_dry2wet == 1), 1, 0)
  wet2wet <- ifelse((is_wet2dry == 0) & (is_dry2wet == 0) & (wet2wet == 1), 1, 0)
  dry2dry <- ifelse((is_wet2dry == 0) & (is_dry2wet == 0) & (wet2wet == 0) & (dry2dry == 1), 1, 0)
  is_wet_new <- ifelse((is_wet2dry == 0) & (is_dry2wet == 0) & (wet2wet == 0) & (dry2dry == 0) & (is_wet_new == 1), 1, 0)
  is_dry_new <- ifelse((is_wet2dry == 0) & (is_dry2wet == 0) & (wet2wet == 0) & (dry2dry == 0) & (is_wet_new == 0) & (is_dry_new == 1), 1, 0)

  # Create new rasters with the same properties as the original rasters
  is_wet2dry_raster <- is_wet
  is_wet2dry_raster[] <- is_wet2dry

  is_dry2wet_raster <- is_dry
  is_dry2wet_raster[] <- is_dry2wet

  wet2wet_raster <- w2w
  wet2wet_raster[] <- wet2wet

  dry2dry_raster <- d2d
  dry2dry_raster[] <- dry2dry

  is_wet_new_raster <- is_wet
  is_wet_new_raster[] <- is_wet_new

  is_dry_new_raster <- is_dry
  is_dry_new_raster[] <- is_dry_new

  # Write the new rasters to the output folder
  writeRaster(is_wet2dry_raster, file.path(output_folder, paste0("is_wet2dry_", i, ".tif")), format = "GTiff")
  writeRaster(is_dry2wet_raster, file.path(output_folder, paste0("is_dry2wet_", i, ".tif")), format = "GTiff")
  writeRaster(wet2wet_raster, file.path(output_folder, paste0("wet2wet_", i, ".tif")), format = "GTiff")
  writeRaster(dry2dry_raster, file.path(output_folder, paste0("dry2dry_", i, ".tif")), format = "GTiff")
  writeRaster(is_wet_new_raster, file.path(output_folder, paste0("is_wet_", i, ".tif")), format = "GTiff")
  writeRaster(is_dry_new_raster, file.path(output_folder, paste0("is_dry_", i, ".tif")), format = "GTiff")
```